

Stabilization of active tissue deformation by a dynamic morphogen gradient

Muhamet Ibrahim^{1,2} and Matthias Merkel^{1,*}

¹*Aix Marseille Univ, Université de Toulon, CNRS, CPT (UMR 7332),
Turing Centre for Living Systems, Marseille, France.*

²*Laboratory of Artificial and Natural Evolution (LANE), Department of Genetics and Evolution,
University of Geneva, 1211 Geneva, Switzerland.*

(Dated: December 23, 2024)

A key process during animal morphogenesis is oriented tissue deformation, which is often driven by internally generated active stresses. Yet, such active oriented materials are prone to well-known instabilities, raising the question of how oriented tissue deformation can be robust during morphogenesis. In a simple scenario, we recently showed that active oriented deformation can be stabilized by the boundary-imposed gradient of a scalar field, which represents, e.g., a morphogen gradient in a developing embryo. Here, we discuss a more realistic scenario, where the morphogen is produced by a localized source region, diffuses across the tissue, and degrades. Consistent with our earlier results, we find that oriented tissue deformation is stable in the gradient-extensile case, i.e. when active stresses act to extend the tissue along the direction of the gradient, but it is unstable in the gradient-contractile case. In addition, we now show that gradient-contractile tissues can not be stabilized even by morphogen diffusion. Finally, we point out the existence of an additional instability, which results from the interplay of tissue shear and morphogen diffusion. Our theoretical results explain the lack of gradient-contractile tissues in the biological literature, suggesting that the active matter instability acts as an evolutionary selection criterion.

I. INTRODUCTION

Oriented tissue deformation is a key process during animal morphogenesis [1], including for instance body axis elongation [2–4] and organ formation [5–10]. In many cases, such tissue deformation is at least in part driven by internally generated active stresses [8, 10–13], and in recent years, deforming tissues have successfully been described as active materials [8, 14–21]. Moreover, to achieve persistent large-scale oriented deformation, tissues need some kind of tissue-wide orientational information, which can be represented for instance by a polar or a nematic field [8, 15, 19, 22, 23]. However, active polar or nematic materials are subject to the well-known Simha-Ramaswamy instability, where an initially globally ordered orientational field loses this order due to active flows [24–26]. This raises the question of how oriented tissue deformation can be stable during animal development.

In animals, oriented tissue deformation can be affected by tissue-scale concentration patterns of proteins, which are often called morphogens. Such morphogen patterns are known to coordinate developmental processes on the tissue or even organism scale [1]. In many cases, they provide positional information [3, 27, 28]. Yet, in some cases they also provide orientational information that defines the axis of active stresses driving oriented tissue deformation [5–7, 12, 29], typically by guiding cellular polarity and cell rearrangements [2, 4, 6, 12, 30]. Such alignment of orientational information with morphogen gradients has recently also been discussed theoretically [31].

In a recent publication [32], we theoretically showed that oriented tissue deformation can be stabilized by morphogen gradients. We used a hydrodynamic model for an active polar material and showed that the gradient of a scalar field, which describes the morphogen gradient, can stabilize the otherwise unstable material. If the scalar field advects with the material flows, we found that the stability of oriented material deformation depends on the coupling between scalar field gradient direction and deformation axis. In the gradient-extensile case, i.e. when anisotropic active stresses act to extend the material along the gradient direction, the scalar field can stabilize the active material deformation. However, in the gradient-contractile case, i.e. when anisotropic active stresses act to contract the material along the gradient direction, the deformation is unstable. However, one could always stabilize even a gradient-contractile system by sufficiently increasing morphogen diffusion.

In our past publication [32], we have created a uniform scalar field gradient in a simple way through appropriate boundary conditions. While providing advantages for analytical calculations, this is quite different from the real mechanism creating morphogen gradients in developing biological tissues [1, 33–36]. Morphogens do indeed advect with tissue flows [37], which we already considered in our previous work [32]. However, they are typically produced by some source region, diffuse across the tissue, and degrade [36, 38]. As a consequence, depending on the source region, this can lead to approximately exponentially decaying [33, 35, 39, 40] or periodic [41, 42] concentration profiles. However, it is not known how such morphogen dynamics would affect oriented deformation of an active material.

In this article, we study the stability of active material deformation when accounting for more realistic mor-

* matthias.merkel@cnrs.fr

phogen dynamics (Figure 1A). We consider an active viscous material with local flow velocity $\mathbf{v}(\mathbf{r}, t)$, where active stresses are defined by the gradient of a morphogen field $c(\mathbf{r}, t)$. We extend our previous work by more realistic morphogen dynamics. Specifically, the morphogen field $c(\mathbf{r}, t)$ is secreted by a source region that is defined by a field $s(\mathbf{r}, t)$, which is conserved and only advects with tissue flows. The morphogen field $c(\mathbf{r}, t)$ not only advects with tissue flows, but also diffuses and degrades at constant rates everywhere.

Using linear stability analysis, we find that also when including more realistic morphogen dynamics, gradient-extensile materials are stable, while gradient-contractile materials are unstable. Yet additionally, we also show that in contrast to a boundary-provided morphogen gradient [32], in the case of a secreted morphogen gradient, a gradient-contractile system can never be stabilized by diffusion. Finally, we find an additional instability in deforming systems for both gradient-extensile and gradient-contractile cases, which arises from the interaction between shear and diffusion, and which is unrelated to the Simha-Ramaswamy active matter instability.

In the following, we first introduce the model in section II. We then study the case of a uniform gradient in both $s(\mathbf{r}, t)$ and $c(\mathbf{r}, t)$ for fixed system size in section III, for which the linear stability can be computed analytically. Next, in section IV, still for fixed system size, we study the more realistic case of a localized source $s(\mathbf{r}, t)$, which gives rise to a non-uniform morphogen gradient $c(\mathbf{r}, t)$. We then discuss the stability of freely deforming systems in section V. Finally, in section VI, we discuss our findings in the context of the biological literature.

II. MODEL

A. Hydrodynamic fields and bulk dynamics

We describe the tissue as a 2D active material, where we consider three interacting hydrodynamic fields: a scalar field $s(\mathbf{r}, t)$, which describes the source, i.e. cells in the tissue which secrete the morphogen; a scalar field $c(\mathbf{r}, t)$, which describes the morphogen concentration; and a vector field $\mathbf{v}(\mathbf{r}, t)$, which describes the tissue flows (Figure 1A). We find that literature values for the respective rates of tissue deformation, morphogen diffusion, and morphogen degradation are of roughly similar orders of magnitude (Figure 1B), suggesting that none of them can be easily neglected, and we thus include all three effects in our model.

The source field $s(\mathbf{r}, t)$, which describes morphogen production, only advects with material flows:

$$\frac{\partial s}{\partial t} + \partial_i(v_i s) = 0, \quad (1)$$

where ∂_i denotes the partial derivative with respect to the spatial coordinate $r_i \in \{x, y\}$. Here and in the following, we label spatial dimensions by Latin indices i, j, \dots and

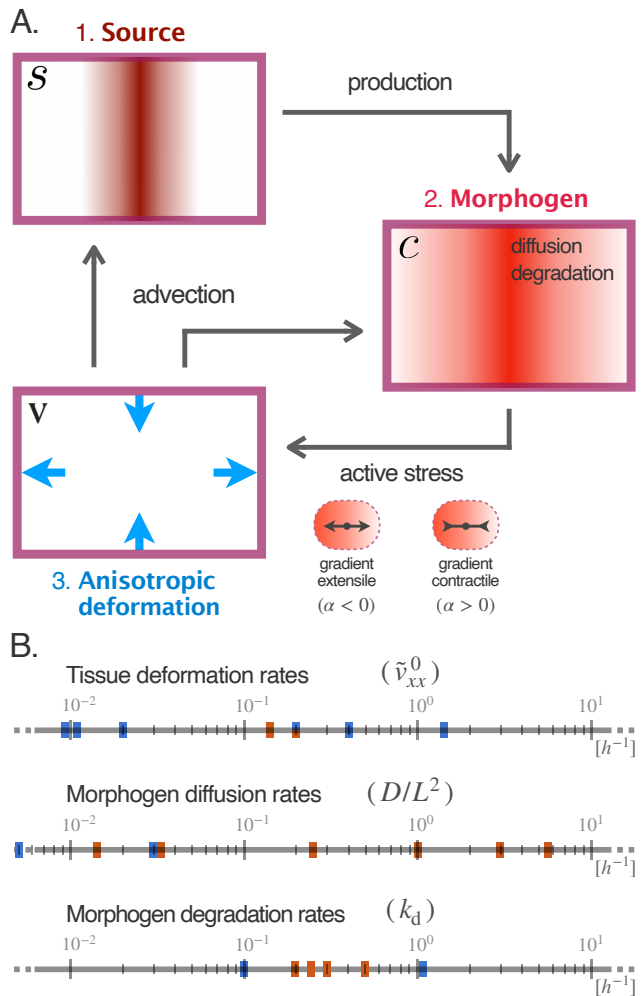


FIG. 1. (A) Hydrodynamic model. A spatially varying source field $s(\mathbf{r}, t)$ secretes a morphogen with concentration $c(\mathbf{r}, t)$, which also diffuses and degrades. The gradient of c creates extensile/contractile active anisotropic stresses, which drive viscous flows with velocity $\mathbf{v}(\mathbf{r}, t)$. These flows affect both source and morphogen fields through advection. (B) Typical orders of magnitude for tissue deformation rates (top), morphogen diffusion rates (middle), and morphogen degradation rates (bottom) from the biological literature. Blue marks are data from the fruit fly *Drosophila melanogaster*, and orange marks are data from zebrafish, *Danio rerio*. Tissue deformation rates in the fruit fly were estimated from: egg chamber [43, 44], dorsal thorax [12], pupal wing [8], hindgut [5, 45], renal tubules [7], and germ-band [11]; and in zebrafish from mesodermal explants [46] and the tailbud [47]. Morphogens: Decapentaplegic in the fruit fly [33, 36, 48]; Cyclops, Squint, Lefty1 and Lefty2 in zebrafish [34, 39].

adopt the Einstein notation of summing over repeated indices.

The morphogen field $c(\mathbf{r}, t)$ follows a generalized conservation equation:

$$\frac{\partial c}{\partial t} + \partial_i(v_i c) = k_p s - k_d c + D \partial_i^2 c. \quad (2)$$

Here, we have introduced production rate k_p , degradation rate k_d , and diffusion coefficient D .

Tissue flows $\mathbf{v}(\mathbf{r}, t)$ are governed by overdamped, incompressible, viscous dynamics:

$$\partial_i \sigma_{ij} = 0, \quad (3)$$

$$\partial_i v_i = 0, \quad (4)$$

where the stress tensor is given by

$$\sigma_{ij} = 2\eta \tilde{v}_{ij} - \Pi \delta_{ij} + \tilde{\sigma}_{ij}^a. \quad (5)$$

Here, η is the shear viscosity, $\tilde{v}_{ij} := (\partial_i v_j + \partial_j v_i - \partial_k v_k \delta_{ij})/2$ is the shear rate tensor, Π is the hydrostatic pressure, and we use the following expression for the active stress $\tilde{\sigma}_{ij}^a$:

$$\tilde{\sigma}_{ij}^a = \alpha \left[(\partial_i c)(\partial_j c) - \frac{1}{2} (\partial_k c)^2 \delta_{ij} \right]. \quad (6)$$

This expression for the anisotropic active stress is the same as in Active Model H [49, 50]. Its direction is determined by the sign of the coefficient α : For $\alpha < 0$, the activity is gradient-extensile, i.e. it acts to extend the material along the local c gradient direction and contract perpendicularly; while for $\alpha > 0$, the activity is gradient-contractile, i.e. it acts to contract the material along the c gradient direction and extend perpendicularly (Figure 1A).

The expression for the active stress, Eq. (6), is motivated by what is known about developing biological tissues. Specifically, anisotropic internal stresses are usually generated by an anisotropic distribution of cytoskeletal elements within cells. Such an anisotropic distribution is created by cell polarity, which in turn can be controlled by morphogen gradients [7, 12, 30, 51, 52]. Here, we assume that the time scales involved in these different couplings are fast enough, so that we directly couple the generated active stresses to the morphogen gradient. Eq. (6) represents the lowest-order term for such a coupling [49].

B. Boundary Conditions

We use periodic boundary conditions, where the periodic box has generally time-dependent dimensions $L_x(t) \times L_y(t)$ and constant area, $L_x(t)L_y(t) = \text{const}$. Throughout this article, we always use one of the following two boundary conditions:

1. We fix the system dimensions L_x and L_y , or
2. we allow the system to freely deform by fixing the externally applied stress to zero, which results in a pure shear deformation of the periodic box. Integration of Eq. (5) implies that the instantaneous box shear rate is

$$\frac{1}{L_x} \frac{dL_x}{dt} = -\frac{\alpha}{4\eta} \int [(\partial_x c)^2 - (\partial_y c)^2] dA, \quad (7)$$

where the integral is over the whole periodic box.

We apply fixed system dimensions in section III and section IV, and study a freely deforming system in section V.

We investigate the stability of two stationary states: (i) a state where a linear source profile s gives rise to a linear morphogen profile c , and (ii) a state where a localized source s generates a spatially decaying morphogen field c . In both cases, the amplitude of the source field is defined by a constant s_b . In case (i), which we study in section III, the boundary conditions are periodic with the exception of the vertical boundaries for the scalar fields s and c , where we set for all $y \in [0, L_y]$:

$$s(0, y) = s(L_x, y) - s_b, \quad (8)$$

$$c(0, y) = c(L_x, y) - \frac{k_p}{k_d} s_b, \quad (9)$$

with fixed s_b . These modified conditions remove the discontinuity that would otherwise appear for linear profiles in s and c at the boundary, and thus ensure that linear s and c profiles can be stationary [32]. In case (ii), which we study in section IV and section V, we use standard periodic boundary conditions without offset.

C. Dimensionless equations

We nondimensionalize the set of equations Eqs. (1)–(9) in the following way:

- We choose the unit of length such that the system area is one $L_x L_y = 1$.
- We choose the unit of the morphogen field c such that $k_p = k_d$.
- We choose the units of time and of the source field s , such that the free deformation rate of a squared system is 1. To this end, we set $|\alpha|/4\eta = 1$, and in case (i) of a linear gradient, we also set $s_b = 1$, while in case (ii) of a non-uniform gradient, we fix s_b as described in section IV (Appendix E1).

The last condition allows to compare the linear stability of systems with different source profiles, because the reference time scale is always the respective free deformation rate.

Rescaled accordingly, the dimensionless equations read:

$$\frac{\partial s}{\partial t} + v_i \partial_i s = 0, \quad (10)$$

$$\frac{\partial c}{\partial t} + v_i \partial_i c = (D \partial_i^2 - k_d) c + k_d s, \quad (11)$$

$$0 = \frac{1}{4} \partial_i^2 v_j - \partial_j \Pi' + \text{sgn}(\alpha) \partial_i [(\partial_i c)(\partial_j c)], \quad (12)$$

$$\partial_i v_i = 0. \quad (13)$$

Here, we have introduced the sign function, $\text{sgn}(\alpha) := \alpha/|\alpha|$, and have set $\Pi' := \Pi + \text{sgn}(\alpha)(\partial_k c)^2/2$. The offset introduced at the boundary conditions in Eqs. (8) and (9) is rescaled to 1 for both scalar fields.

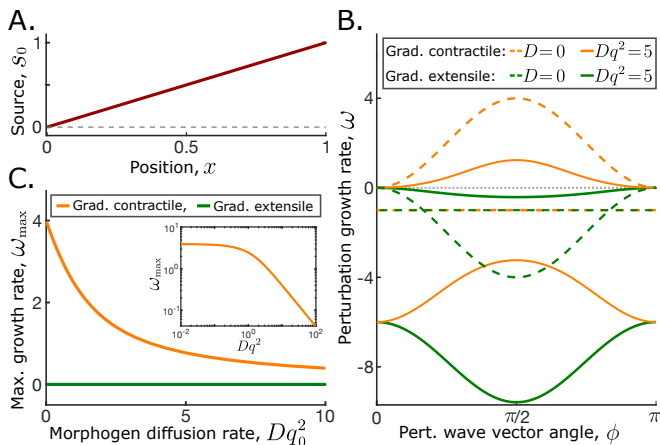


FIG. 2. Stability of a fixed-size system with a linear source profile: gradient-contractile systems (orange) are unstable, whereas gradient-extensile systems (green) are marginally stable. (A) The linear source profile, $s_0(x) = x$ in dimensionless units. In the stationary state, $c_0(x) = s_0(x)$. (B) The perturbation growth rates ω depending on wave vector angles ϕ . There are 2 branches for each of the 4 cases reported (see legend). (C) Effect of morphogen diffusion rate Dq_0^2 (with $q_0 = 2\pi$) on the maximal perturbation growth rates ω_{\max} of the linear systems. Inset: same data in log-log scaling for the gradient-contractile case.

III. LINEAR SOURCE PROFILE

To build intuition, we study for fixed box dimensions $L_x = L_y = 1$ the linear stability of a stationary state with linear spatial profiles in s and c (Figure 2A), given by:

$$s_0 = x, \quad c_0 = x, \quad \mathbf{v}_0 = \mathbf{0}. \quad (14)$$

There are no flows in the stationary state, because the gradient of c is homogeneous, and thus the active stress is homogeneous across the system of fixed dimensions.

In this case, linear stability can be computed analytically. When we add a small perturbation around this state,

$$s = x + \delta s, \quad c = x + \delta c, \quad \mathbf{v} = \delta \mathbf{v}, \quad (15)$$

and linearize the dynamics, only constant prefactors occur. As a consequence the solutions in $(\delta s, \delta c, \delta \mathbf{v})$ are spatial Fourier modes with wave vectors $\mathbf{q} = q(\cos \phi, \sin \phi)$, whose amplitudes grow or shrink exponentially with time t (Appendix D).

We first discuss the limit without diffusion, $D = 0$. When we subtract the linearized versions of the source dynamics, Eq. (10), from the linearized version of the morphogen dynamics, (11), we obtain:

$$\frac{\partial}{\partial t}(\delta c - \delta s) = -k_d(\delta c - \delta s). \quad (16)$$

Thus, any difference between morphogen field c and source field s decays at rate k_d (dashed horizontal lines in

Figure 2B). In addition, the combination of morphogen dynamics and generated active flows, Eqs. (11)–(13), leads to the same results as for a single scalar field discussed in earlier publications [32, 50] (Appendix D1). This means that the perturbation growth rate ω_{act} due to the active flows depends on the angle of the Fourier mode ϕ as $\omega_{\text{act}} := 4 \text{sgn}(\alpha) \sin^2 \phi$, as indicated by the dashed curves in Figure 2B. Thus, without diffusion, the system is marginally stable in the gradient-extensile case, where the maximal perturbation growth rate is zero (green dashed curve), and unstable in the gradient-contractile case, where the maximum perturbation growth rate is strictly positive (orange dashed curve).

Even in the presence of diffusion, $D > 0$, a gradient-contractile system remains always unstable, although the maximal perturbation growth rate decreases with diffusion (orange curve in Figure 2C & inset). This is in contrast to earlier findings for a system with a single scalar field c without source, where we found that diffusion *can* stabilize the system in the gradient-contractile case. To understand where the difference comes from, we consider the limit of very large D . The linearized version of the morphogen dynamics, Eq. (11), in Fourier space reads:

$$\frac{\partial \delta c}{\partial t} + \delta v_x = -(Dq^2 + k_d) \delta c + k_d \delta s. \quad (17)$$

The flow field $\delta \mathbf{v}$ enters on the left-hand side due to advection, where $\partial_x c_0 = 1$ in dimensionless units. The flow $\delta \mathbf{v}$ is actively created by the morphogen field itself through Eqs. (12) and (13), and their x component in Fourier space reads: $\delta v_x = -\omega_{\text{act}} \delta c$, with the active flow time scale ω_{act} introduced before (Appendix D). Denoting the minimal non-zero wave vector magnitude in our system by q_{\min} , we take the limit where Dq_{\min}^2 is much larger than all other relevant time scales in the system. In this case, according to Eq. (17), the Fourier amplitudes δc for each wave vector relax adiabatically fast towards

$$\delta c \simeq \frac{k_d}{Dq^2} \delta s. \quad (18)$$

This effectively corresponds to a system where we again just have a single scalar field s , which advects with active tissue flows \mathbf{v} , but does *not* diffuse. The active tissue flows are generated by the perturbations of c , and their x component is given by $\delta v_x = -\omega_{\text{act}} \delta c \simeq -(\omega_{\text{act}} k_d / Dq^2) \delta s$. Inserting this in the linearized version of the source dynamics in Fourier space, we get:

$$\frac{\partial \delta s}{\partial t} = -\delta v_x = \frac{\omega_{\text{act}} k_d}{Dq^2} \delta s = \frac{4k_d \text{sgn}(\alpha) \sin^2 \phi}{Dq^2} \delta s. \quad (19)$$

Thus, the sign of the growth rate of δs just depends on the sign of α . As a consequence, the system is unstable for a gradient-contractile system ($\alpha > 0$), even in the limit of a large diffusion constant. The reason for this is that the source field itself advects with the active flows, but does not diffuse. For the same reason, any gradient-extensile system remains only marginally stable even in the presence of morphogen diffusion.

IV. LOCALIZED SOURCE PROFILE

In the following, we discuss how the linear stability changes when the source profile is not linear but instead localized to some region of finite width w . This is motivated by what we know of developing biological tissues [1, 33, 38, 42]. In this section, we discuss a system of fixed size, while in section V, we discuss a freely deforming system.

As initial state, we use a source profile that is similar to a *von Mises* distribution, which is a generalization of a Gaussian to periodic boundary conditions:

$$s_0(\mathbf{r}) = s_b \left[\exp\left(\frac{\cos(q_0 x)}{(q_0 w)^2}\right) - \exp\left(-\frac{1}{(q_0 w)^2}\right) \right] \quad (20)$$

with $q_0 = 2\pi/L_x$. Here, w is a parameter that adjusts the width of the source region, and the second term in Eq. (20) ensures that $s_0(\mathbf{r})$ is zero at its minimum. As initial c_0 field, we choose the c field that is stationary in the absence of flows for s_0 given by Eq. (20). In Fourier space:

$$c_0(\mathbf{q}) = \frac{k_d}{k_d + Dq^2} s_0(\mathbf{q}). \quad (21)$$

Thus, for $D = 0$, morphogen and source profiles coincide, and examples for $s_0(x) = c_0(x)$ for different w values are shown in Figure 3A. Meanwhile, finite diffusion $D > 0$ smoothens the morphogen profile $c_0(x)$ as compared to the source profile $s_0(x)$ (Figure 4A).

In this initial state, there are no flows in the system, $\mathbf{v}_0 = \mathbf{0}$. This is because the active stress in this case is parallel to the x axis and homogeneous along the y axis, because of incompressibility, and of the fixed system size, which together imply that there are no Stokes flows (Appendix B 2).

For a localized source, we study linear stability numerically. This is because the non-uniform gradient in the c field creates non-constant coefficients in the linearized perturbation dynamics. As a consequence, the linearized dynamics in Fourier space now includes Fourier-space convolutions of the stationary profile c_0 and the morphogen perturbations δc (Appendix C 2). Because of this, while the eigen modes of the linearized dynamics still grow or shrink exponentially with time, they are not single Fourier modes any more. We thus compute the perturbation eigen modes and their respective growth rates numerically.

For the case without diffusion, $D = 0$, we plot in Figure 3B, C the growth rates ω_m of the different eigen modes m , where Figure 3B is for a gradient-contractile system and Figure 3C for a gradient-extensile system. For each eigen mode, the growth rates are plotted over their respective mean wavenumber $\langle n \rangle_m$, which we define as

$$\langle n \rangle_m := \frac{1}{2\pi} \frac{\sum_{\mathbf{q}} |\delta c_m(\mathbf{q})| q}{\sum_{\mathbf{q}} |\delta c_m(\mathbf{q})|}, \quad (22)$$

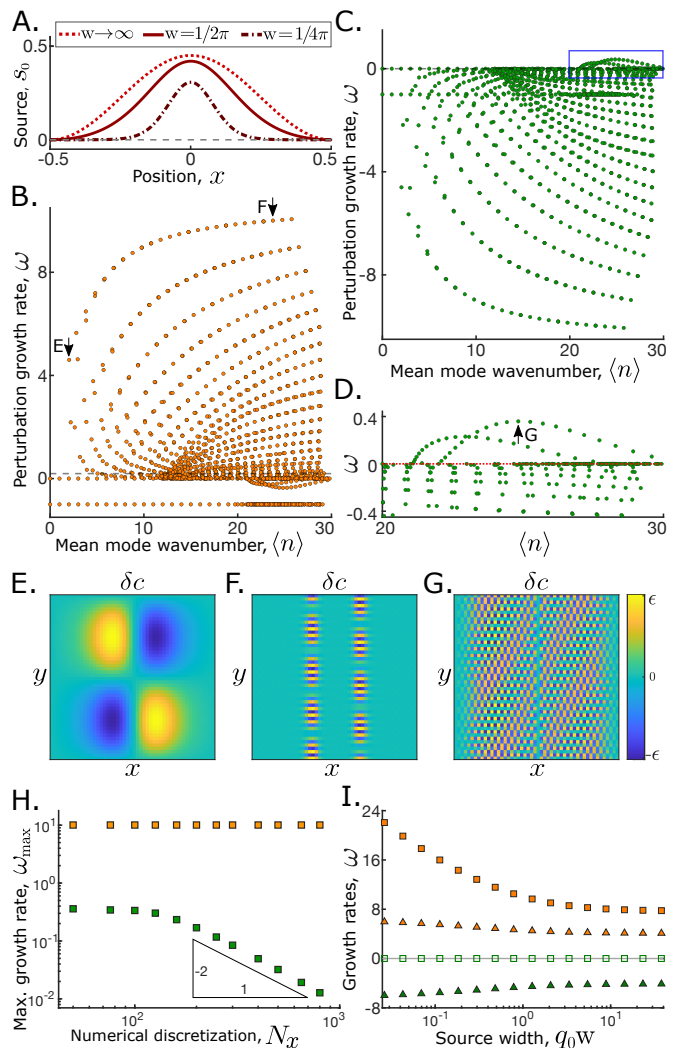


FIG. 3. Stability of a fixed-size system with a localized source profile and a non-diffusive morphogen, $D = 0$. (A) The localized source profile $s_0(x)$ from Eq. (20) for different values of the source width w . (B,C) Growth rates ω_m of perturbation modes depending on their mean wavenumber $\langle n \rangle_m$ for a system with $w = 1/2\pi$, for (B) a gradient-contractile and a (C) gradient-extensile system. The eigenvalue problem was solved numerically as described in Appendix C 3. (D) Zoomed region of panel C displaying high-wavenumber perturbation modes with $\omega > 0$, which we interpret as numerical artifacts, due to the spatial discretization (see main text, Appendix E 2, and panel G). (E-G) Morphogen field perturbation $\delta c(\mathbf{r})$ for three different eigen modes (as indicated in panels B and D). (E) δc mode for small wavenumber $\langle n \rangle$, with positive growth rate in the gradient-contractile case. (F) Typical δc mode with high $\langle n \rangle$ and high growth rate in the gradient-contractile case. (G) Typical δc mode with numerically obtained positive growth rate in the gradient-extensile system. (H) Maximal growth rate ω_{\max} in gradient-contractile and -extensile systems depending on the numerical discretization, N_x . For gradient-extensile systems, this growth rate decreases as $\omega_{\max} \sim N_x^{-2}$. (I) Perturbation growth rate depending on the source width w . Squares indicate ω_{\max} , whereas triangles indicate the growth rate of perturbation modes in with small $\langle n \rangle$ (see main text and panel E).

in dimensionless units (i.e. $L_x = L_y = 1$), and where $\delta c_m(\mathbf{q})$ denotes the morphogen field part of eigen mode m in Fourier space. For the gradient-contractile case, [Figure 3B](#), we thus find that also for a non-uniform source the system is unstable, since there are many eigen modes with a positive growth rate $\omega_m > 0$.

Surprisingly, [Figure 3C](#) seems to suggest that also gradient-extensile systems are unstable in this case, because there are modes with a positive growth rate (see magnified region in [Figure 3D](#)). However, these modes all have almost maximal wave number $\langle n \rangle_m \gg 1$ ([Figure 3D, G](#)). We thus wondered whether these positive growth rates might a numerical artifact, for instance due to the numerical discretization of the source and morphogen fields. To test this, we quantified the maximum of all growth rates ω_m for increasing numerical resolution in [Figure 3H](#). We find that for the gradient-extensile case (green squares) the maximal growth rate decreases as $\omega_{\max} \sim N_x^{-2}$ with the numerical resolution in x direction, N_x , while it remains largely constant for the gradient-contractile case (orange squares). This indicates that the positive growth rates of the large- $\langle n \rangle_m$ modes in the gradient-extensile case shown in [Figure 3C](#) inset are due to a numerical discretization artifact, without which the maximal growth rate in the gradient-extensile case would be zero. We independently confirm this further in appendix [Appendix E 2](#).

Next, we study for $D = 0$ how the system's stability depends on the source width w ([Figure 3I](#)). The gradient-contractile system (orange symbols) is always unstable, where the squares in [Figure 3I](#) show the maximum growth rate, which decreases with source size, but approaches a positive value for $w \rightarrow \infty$. As indicated by [Figure 3B](#), this maximal growth rate can correspond to a mode m with a large wavenumber $\langle n \rangle_m$ ([Figure 3F](#)). However, in biological tissues there is a natural upper wave vector cutoff, provided for instance by the cell size. Thus, to test in how far our results are still valid in the presence of some wave vector cutoff, we also indicate the growth rates of a small-wavevector mode. We selected the mode with $\langle n_x \rangle_m \neq 0$ and $\langle n_y \rangle_m \neq 0$ that has the smallest $\langle n \rangle_m$, where we used $\langle n_i \rangle_m := \left(\sum_{\mathbf{q}} |\delta c_m(\mathbf{q})| q_i \right) / \left(2\pi \sum_{\mathbf{q}} |\delta c_m(\mathbf{q})| \right)$. We find that also this small-wavevector mode has a positive growth rate for all source widths, which also approaches a finite value for $w \rightarrow \infty$ (orange triangles in [Figure 3E](#)). Thus, we expect the material to be unstable even in the presence of some upper wave vector cutoff. In contrast, the gradient-extensile system (green symbols) is always marginally stable, where the squares show again the maximum growth rate. The squares are open to indicate that we ignored any modes with large wavevector and positive growth rates based on our discussion in the previous paragraph.

Finally, we study how the system stability depends on the diffusion coefficient D . In this case, gradient-extensile systems are still marginally stable for any $D > 0$ ([Fig-](#)

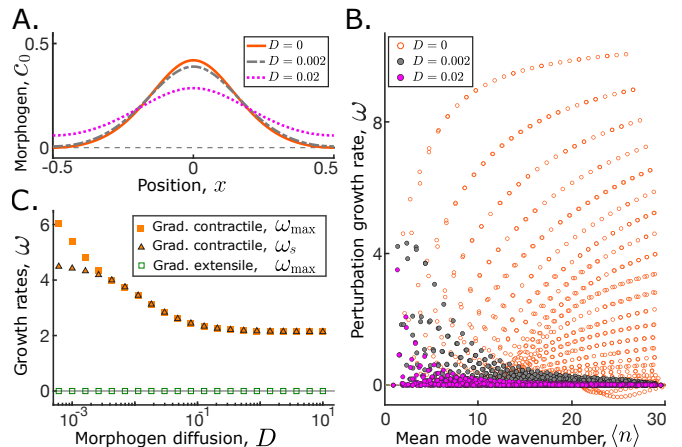


FIG. 4. Effect of finite morphogen diffusion, $D > 0$, on the stability of the fixed-size system with a localized source. Diffusion can not stabilize a gradient-contractile system. (A) Stationary morphogen profiles $c_0(x)$ for different diffusion coefficients, where $w = 1/2\pi$. (B) Perturbation growth rates of gradient-contractile systems for the three diffusion coefficients indicated in panel A. (C) Perturbation growth rates with increasing D . Squares indicate maximal growth rates ω_{\max} and triangles indicate growth rates of modes in the small $\langle n \rangle$ limit, ω_s .

[ure 4C](#)). They are not further stabilized by diffusion for the same reason as for a linear source profile: any perturbation with $\phi = 0$ in the source field neither induces any flows, nor can it “diffuse away”.

For gradient-contractile systems, diffusion decreases the growth rates of the large-wavevector modes ([Figure 4B](#)). Thus, for large enough diffusion constant, the system's fastest growing mode becomes the small-wavevector mode. Hence, the maximum growth rate (orange squares in [Figure 4C](#)) overlaps with the growth rate of the small-wavevector mode (orange triangles) for $D \gtrsim 10^{-2}$. Remarkably, while for a linear source profile, a sufficiently high diffusion coefficient could bring down the maximal perturbation growth rate arbitrarily close to zero ([Figure 2C](#), Eq. (19)), this is not possible any more for a localized source. Instead, for a localized source, the maximum perturbation growth rate is always larger than ≈ 2 in units of the free deformation rate ([Figure 4C](#)).

V. FREELY DEFORMING SYSTEM

Here we study the linear stability of a system with a localized source s_0 , Eq. (20), under free deformation. In this case, even for homogeneous shear deformation, the source profile s_0 is not stationary, but becomes distorted due to advection with the pure shear deformation ([Figure 5A](#)).

However, the source profile is stationary with respect to “co-deforming” coordinates. Following our earlier work [32], we define the co-deforming coordinates, $\bar{\mathbf{r}} = (\bar{x}, \bar{y})$, based on the lab-frame coordinates $\mathbf{r} = (x, y)$ by

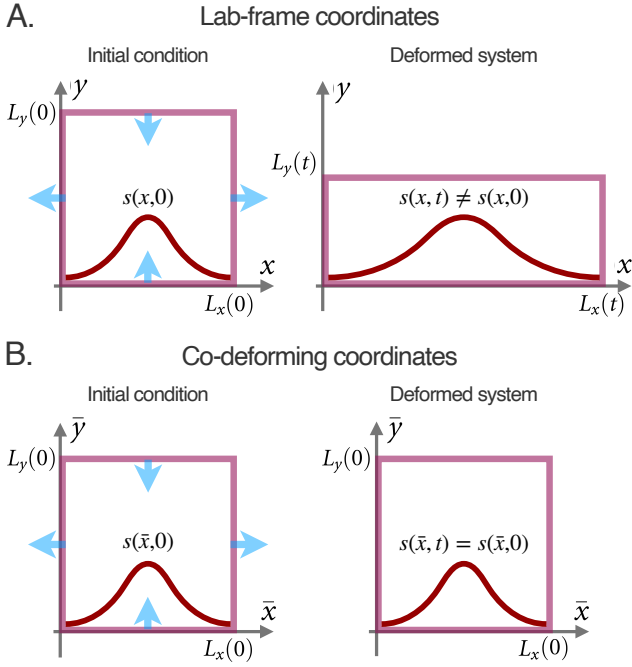


FIG. 5. We introduce co-deforming coordinates to study a deforming system, Eqs. (23) and (24). (A) In lab-frame coordinates, a localized source $s(\mathbf{r}, t)$ is not stationary when the system is deforming affinely, because its width changes proportionally with the system dimension L_x due to advection. (B) However, in co-deforming coordinates, the localized source $s(\bar{\mathbf{r}}, t)$ remains stationary under affine deformation.

rescaling both axes:

$$\bar{x} := \frac{L_x(0)}{L_x(t)}x = l_x^{-1}(t)x \quad (23)$$

$$\bar{y} := \frac{L_y(0)}{L_y(t)}y = l_x(t)y, \quad (24)$$

where $l_x(t) := L_x(t)/L_x(0)$ is the box shear. Moreover, we also introduce a flow field in co-deforming coordinates, $\bar{\mathbf{v}}(\bar{\mathbf{r}})$, which corresponds to non-affine flows that may occur in addition to the pure shear deformation of the periodic box (Appendix A 3). Thus, for $\bar{\mathbf{v}} = \mathbf{0}$ the system deforms affinely. In this case, the source field $s_0(\bar{\mathbf{r}})$ is stationary with respect to the co-deforming coordinates (Figure 5B).

A. No morphogen diffusion, $D = 0$

Without diffusion, the morphogen concentration given by $c_0(\bar{x}) = s_0(\bar{x})$ is stationary with respect to the co-deforming coordinates, and the system deforms affinely, $\bar{\mathbf{v}}_0 = \mathbf{0}$. This is again due to the homogeneity of c_0 (and thus the active stresses) in y direction combined with incompressibility (Appendix B 2).

System dimension dynamics. The dynamics of system dimension L_x , and thus box shear l_x , is given

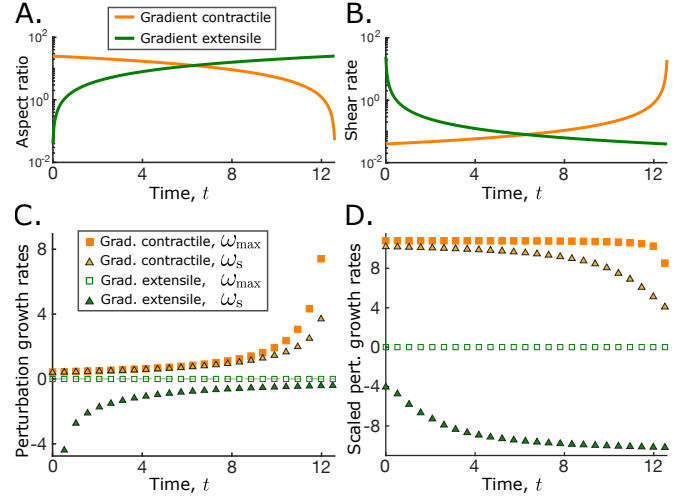


FIG. 6. Stability of a freely deforming system with a non-diffusive morphogen, $D = 0$. (A) Time evolution of aspect ratios of a gradient-extensile system (green) and a gradient-contractile system (orange) starting from $L_x(0)/L_y(0) = 0.04$ and $L_x(0)/L_y(0) = 25$, respectively. (B) The corresponding absolute values of the shear rates of the systems in panel A. (C) Instantaneous perturbation growth rates over time for the systems in panel A. Square symbols display the maximal growth rates ω_{\max} , whereas triangles display growth rates of small-wavenumber perturbations ω_s (see Figure 3E). (D) Same as in panel C, where the perturbation growth rates are rescaled by the instantaneous shear rate.

by Eq. (7). Thus, in the stationary state, the shear rate is essentially given by the integral over $(\partial_x c_0)^2$. Because the morphogen profile, c_0 , is stationary in co-deforming coordinates, we have that for varying system size, $(\partial_x c_0)^2 \sim 1/l_x^2$. So, using dimensionless units (section II C), we can write

$$\frac{1}{l_x} \frac{dl_x}{dt} = -\frac{\text{sgn}(\alpha)}{l_x^2 L_x^2(0)}. \quad (25)$$

The solution of this is:

$$l_x(t) = \sqrt{1 - \frac{2\text{sgn}(\alpha)t}{L_x(0)^2}}. \quad (26)$$

Thus, gradient-extensile systems ($\alpha < 0$) deform slower and slower due to the widening of the morphogen profile (green curves in Figure 6A,B). Meanwhile, gradient-contractile systems ($\alpha > 0$) deform faster and faster over time due to the compression of the morphogen profile, until the deformation rate diverges at some critical time point $t_{\text{crit}} = L_x^2(0)/2$ (orange curves in Figure 6A,B).

Perturbation growth rates. Without diffusion, the dynamics of source and morphogen perturbations, δs and δc , are independent of the box shear perturbation, δl_x (Eqs. (C4) and (C5) in Appendix C 1), but they still do depend on box shear $l_x(t)$ itself. Thus, to characterize the system's stability over time, we can use our linear stability analysis for the fixed-size system (section IV and Figure 3), where we use the time-dependent l_x according to

Eq. (26). The results are shown in Figure 6C: As in section IV and Figure 3, the gradient-contractile systems are always unstable, where even their smallest-wavevector perturbation grows (orange symbols), while the gradient-extensile system is always marginally stable with a decaying smallest-wavevector perturbation (green triangles). We moreover observe that for gradient-contractile systems, the perturbation growth rates become substantially larger at late times, where l_x is small. Meanwhile, for gradient-extensile systems, the magnitude of the decay rates is substantially larger at earlier times, where again l_x is small. This is likely due to the stronger localization of the source region due to the smaller l_x ; indeed, in Figure 3I we showed that the magnitudes of the perturbation growth rates are larger for smaller source sizes w . To better compare to the box shear rate, in Figure 6D we normalize these perturbation growth rates by the instantaneous box shear rate from Figure 6B. We find that the perturbation growth rate magnitudes normalized by the instantaneous shear rates vary much less over time, and is typically on the order of 10, both for gradient-contractile and -extensile systems. They only become a little smaller for systems with small l_x (i.e. late times for gradient-contractile systems, and early times for gradient-extensile systems). Figure 6D allows to predict the expected perturbation growth rates for a biological system of known instantaneous free deformation rate.

B. Finite morphogen diffusion, $D > 0$

In a fixed-size system with the source field s_0 given by Eq. (20) and with $D > 0$, the interaction between production, diffusion, and degradation allowed for existence of a stationary state (section IV). However, when such a system is allowed to freely deform, it does not reach a stationary state – not even in co-deforming coordinates. This is because diffusion as observed in co-deforming coordinates depends on box shear l_x through the transformation rules in Eqs. (23) and (24). Thus, as a consequence of the permanently changing l_x , there is no stationary state in the freely deforming case.

The system state $\vec{z}(t) = [s(\vec{r}, t), c(\vec{r}, t), l_x(t)]$, which combines source and morphogen profiles in co-deforming coordinates with box shear, constantly evolves through Eqs. (7) and (10)–(13), which we summarize here as $d\vec{z}/dt = \vec{F}(\vec{z})$. As initial condition, we use the source profile s_0 from Eq. (20), and the corresponding morphogen profile c_0 that *would* be stationary in a fixed system, Eq. (21). To simplify our discussion here, we will focus on the limit $w \rightarrow \infty$, where the source $s_0(\mathbf{r})$ given by Eq. (20) corresponds to a cosine profile, $s_0(\mathbf{r}) \sim \cos(2\pi x/L_x) + 1$. The corresponding morphogen profile is then also a cosine profile.

System size dynamics. In a gradient-extensile system, we observe that the aspect ratio increases over time as expected (green curve in Figure 7A). However, the shear rate first increases and then decreases (green

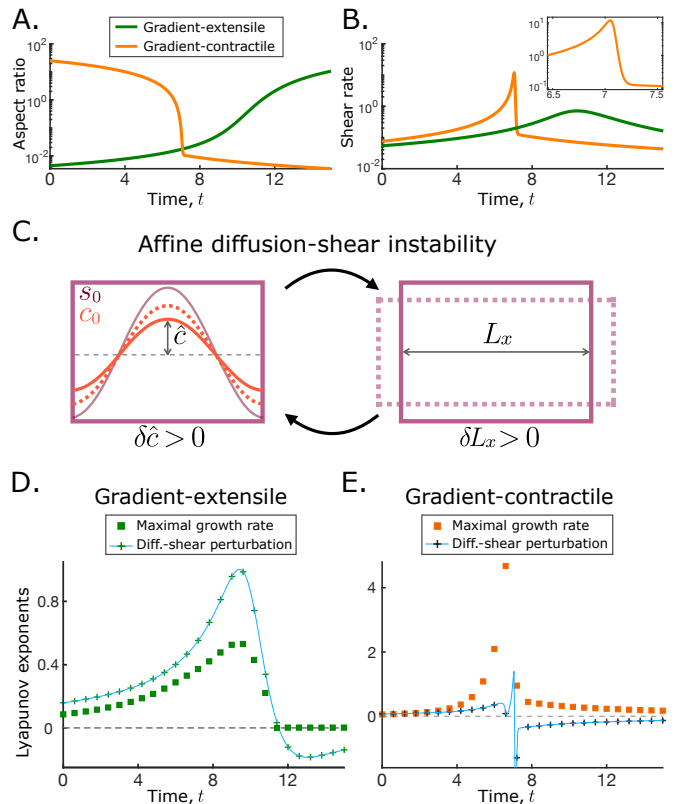


FIG. 7. Stability of a freely deforming system with a diffusive morphogen, where we set $D = 10^{-2}$ and in the limit $w \rightarrow \infty$, where the source has a cosine shape. (A) Aspect ratio over time for the gradient-extensile (green) and contractile (orange) systems, starting at initial aspect ratios of $L_x(0)/L_y(0) = 1/225$ and $L_x(0)/L_y(0) = 25$, respectively. (B) The corresponding absolute values of the shear rates of the systems in panel A. Inset: zoomed around the sharp drop in the gradient-contractile case. (C) Illustration of the affine diffusion-shear instability: diffusion reduces the amplitude \hat{c} of the morphogen field, but a larger L_x decreases the effectiveness of diffusion. Thus, a larger L_x leads to a larger \hat{c} , which in turn increases active shear and thus L_x . (D) Local Lyapunov exponents (LLE) for the gradient-extensile system over time. Green crosses indicate the numerically computed LLE of the affine diffusion-shear perturbation with the largest growth rate, and the blue curve displays the analytical prediction according to Eq. (F8) in Appendix F 2 a. Green squares denote the maximal LLE of all other perturbations. (E) The same results as in panel D, but for the gradient-contractile system.

curve in Figure 7B), in contrast to the case without diffusion, where it monotonically decreases (Figure 6B). For gradient-contractile systems, we observe a much more erratic system size behavior (orange curves in Figure 7A,B). In particular, the shear rate shows a transient, but pronounced peak before quickly switching to much slower dynamics (Figure 7B inset). We discuss the reason for these l_x dynamics in detail using scaling arguments in Appendix F 1.

Local Lyapunov exponents. We next discuss the

robustness of the system’s dynamics. Because there is no stationary state in the $D > 0$ case, we decided to quantify the local Lyapunov exponents, which characterize whether and how quickly two slightly different solutions, \vec{z} and \vec{z}' , converge or diverge. The difference between both, $\delta\vec{z} := \vec{z}' - \vec{z}$, follows the dynamics $d\delta\vec{z}/dt = J(\vec{z}) \cdot \delta\vec{z}$, where $J(\vec{z})$ is the Jacobian of $\vec{F}(\vec{z})$. The local Lyapunov exponents at \vec{z} are then given by the eigenvalue spectrum of $J(\vec{z})$. When applied to a stationary state, this approach coincides with linear stability analysis.

We first briefly discuss the local Lyapunov exponents in the limit of no diffusion, $D = 0$ (previous section, [section V A](#)). For $D = 0$, the linearized dynamics of source and morphogen, Eqs. (C4) and (C5) (Appendix C 1), do not depend on the perturbation of the box shear, δl_x . Thus, the perturbation dynamics of s and c decouples from that of l_x , and most of the Lyapunov spectrum is what we already discussed in the previous section. The remaining eigenvalue of the local Lyapunov spectrum is given by the system size perturbation dynamics:

$$\frac{d\delta l_x}{dt} = \frac{\text{sgn}(\alpha)}{l_x^2(t)L_x^2(0)}\delta l_x. \quad (27)$$

The prefactor in this equation is positive for a gradient-contractile system and negative for a gradient-extensile system. Hence, for $D = 0$, the gradient-contractile system has positive local Lyapunov exponents, i.e. the system dynamics strongly depends on the initial conditions. Meanwhile for gradient-extensile systems, the maximal local Lyapunov exponent is zero, and so the system dynamics depends less strongly on the initial conditions.

For $D > 0$, the equations defining the linearized dynamics, Eqs. (C4)–(C6), are all coupled to each other and the full Jacobian needs to be diagonalized in order to obtain the local Lyapunov exponents. At each time point of the trajectory $\vec{z}(t)$, we plot the maximal Lyapunov exponent in [Figure 7D,E](#). Here, we first discuss the gradient-extensile case. In the previous section, for $D = 0$, we found that the maximal growth rate of all perturbation modes $\delta\vec{z}$ was zero ([Figure 6C](#)), at least in the limit of an infinitely fine spatial discretization (Appendix E 2). In contrast, we find here that the maximal perturbation growth rate can be positive (green crosses in [Figure 7D](#)). Yet, at later times, when l_x is larger, the maximal growth rate becomes zero, as before (green squares in [Figure 7D](#)). This fastest growing perturbation mode (green crosses in [Figure 7D](#)), which we call here “affine diffusion-shear perturbation”, is different from the active scalar matter instability [[32](#), [50](#)]. It does not affect the non-affine part of the flow field, \vec{v} or the source field s . Moreover, the morphogen profile keeps its cosine shape, and only its amplitude \hat{c} and the box shear l_x are affected by the perturbation. The positive growth rate of this mode arises from the fact that diffusion diminishes the amplitude of the morphogen cosine profile, \hat{c} . Thus, increasing l_x by some positive amount δl_x decreases the effect of diffusion, which acts to increase \hat{c} and thus the integrated

squared morphogen gradient, which in turn acts to further increase l_x ([Figure 7C](#)). In Appendix F 2 a, Eq. (F8), we obtain the analytical prediction of the growth rate of this mode (blue dashed line in [Figure 7D](#)), which matches our numerical results (green crosses). From our analytical prediction, we find that the system is unstable as long as the diffusion length $\lambda := \sqrt{D/k_d}$ is larger than L_x , or more precisely $\lambda > L_x/2\pi\sqrt{3}$ (Appendix F 2 a).

For the gradient-contractile case, we found for $D = 0$ several modes with a positive growth rate. For $D > 0$ this is still true (orange squares in [Figure 7E](#)), and – like in the gradient-extensile case – we again have an eigenmode of the Jacobian that is an affine diffusion-shear perturbation, i.e. it does not affect source field and non-affine flows (black crosses in [Figure 7E](#) compare predicted growth rate marked by the blue line).

Finally, we studied how the instability due to the affine diffusion-shear perturbation is changed for the general case of finite source width w , and we find that this perturbation has a positive growth rate whenever the order of magnitude of the diffusion length becomes larger than the source width, $\lambda \gtrsim w$ (Appendix F 2 b).

VI. DISCUSSION

In developing animals, biological tissues can undergo active anisotropic deformation [[1](#)]. However, classical active matter results predict that such deformations are unstable under certain conditions [[24](#), [25](#), [50](#)]. In several systems, the local direction of active tissue deformation is controlled by the gradient of a protein concentration field [[7](#), [12](#), [30](#)]. Such proteins are called morphogens. They are typically produced by the cells in a localized source region of the tissue, and they can form gradients through diffusion and degrade [[1](#)]. However, both morphogen pattern and source region are also advected by the flows generated by the active deformation [[37](#)]. Here, we studied the stability of a system which includes source field, morphogen field, and morphogen-gradient-controlled active tissue deformation. Similar to what we found earlier without explicit source region [[32](#)], we find that systems where the active stresses are gradient-extensile can be marginally stable, while gradient-contractile systems are always unstable. This is consistent with an observed abundance of gradient-extensile systems in the biological literature [[3](#), [5](#), [7](#), [29](#), [41](#), [44](#), [46](#), [51](#), [53](#), [54](#)] and the virtual absence of gradient-contractile systems (also discussed in [[55](#)]), suggesting that the instability discussed here may act as an evolutionary selection criterion.

We further find that in the gradient-contractile case, neither degradation nor diffusion can stabilize the system. Degradation only acts – in conjunction with production – to decrease the difference between morphogen and source fields. Meanwhile the system is still subject to the instability. Also, while diffusion can decrease the growth rates of perturbations in the gradient-contractile case, we find that it never suffices to fully stabilize the sys-

tem. This is because both morphogen and source fields advect with the active flows, while only the morphogen diffuses. In the case of a linear source profile, the maximal perturbation growth rate could become arbitrarily small for sufficiently large diffusion coefficient. However, in the case of a localized source, the maximal perturbation growth rate is always at least ≈ 2 times the free deformation rate.

We also identify another instability that is not related to the classical active matter instability, which we call ‘‘affine diffusion-shear instability’’, and which also appears in the gradient-extensile case. More precisely, this instability corresponds to a positive local Lyapunov exponent of a dynamically changing state. It arises from the interplay between the pure shear of the system and the amplitude of the morphogen profile, and in tissues with a localized source whose width is much smaller than the morphogen diffusion length $\sqrt{D/k_d}$. In this case, the extent of the morphogen profile is defined by the diffusion length, while its amplitude is defined by the width of the source region. As a consequence, when the system shear is perturbed to be slightly larger, and consequentially the source width increases, thus the amplitude of the morphogen field increases, which promotes a faster shear. In the context of deforming biological tissues, a positive Lyapunov exponent means that the time-dependent deformation of such tissues is expected to be not very reproducible. In many developing tissues, the morphogen profile has a larger extent than the source region [1, 5, 33], and our work suggests that this instability should occur. This raises the question of how this instability is prevented in developing systems. One possibility might be that there is a saturation in the active stresses as a function of the magnitude of the morphogen gradient. Such a saturation could be mediated for instance through cell polarity [32]. Whether this could be sufficient to suppress this instability is an interesting question for future research.

Our study further motivates experiments, and a key question is whether there are at all any gradient-contractile biological systems. There are many systems where morphogen profiles are known to be necessary for active anisotropic tissue deformation. However, it is most often not yet known whether the gradient of the morphogen controls the directionality or only the magnitude of the active stresses. Thus, experiments are needed that disentangle both. For instance, to modify the direction of the morphogen pattern while keeping the overall magnitude the same, one could combine combine null-mutants with a graded over-expression [30] or the external supply of a gradient, e.g. through morphogen-soaked beads [1, 27]. We believe that combining insights from active matter theory with experiments in this way will help decode the biological mechanisms underlying oriented tissue deformation and their robustness.

ACKNOWLEDGMENTS

We thank the Centre Interdisciplinaire de Nanoscience de Marseille (CINaM) for providing office space. The project leading to this publication has received funding from France 2030, the French Government program managed by the French National Research Agency (ANR-16-CONV-0001), and from the Excellence Initiative of Aix-Marseille University - A*MIDEX. This project was also supported by the grant RobustTissue attributed to M.M. by the French National Research Agency (ANR-22-CE30-0039).

Appendix A: Co-deforming coordinates

1. Definition

Following Ref. [32], we introduce the co-deforming coordinate system, $(\bar{\mathbf{r}}, \bar{t}) = (\bar{x}, \bar{y}, \bar{t})$, to analytically solve the linearized dynamics of systems under pure shear deformation.

The co-deforming coordinates map to the lab coordinates $(\mathbf{r}, t) = (x, y, t)$ in the following way:

$$r_i = s_{ij}(\bar{t})\bar{r}_j \quad (\text{A1})$$

$$t = \bar{t}, \quad (\text{A2})$$

where $\mathbf{s}(\bar{t})$ is a time-dependent shear tensor, given by

$$\mathbf{s}(\bar{t}) = \begin{pmatrix} l_x(\bar{t}) & 0 \\ 0 & l_x^{-1}(\bar{t}) \end{pmatrix}. \quad (\text{A3})$$

Thus, while at some time t , lab coordinates range from $0 \leq x < L_x(t)$ and $0 \leq y < L_y(t)$, co-deforming coordinates map these affinely to the box dimensions at time zero, with $0 \leq \bar{x} < L_x(0)$ and $0 \leq \bar{y} < L_y(0)$.

Note that for fixed system dimensions, where $L_x(t) = L_x(0)$, and thus $l_x(t) = 1$, both, co-deforming and lab coordinates coincide, $\bar{\mathbf{r}} \equiv \mathbf{r}$.

2. Partial derivatives

As a direct consequence of Eqs. (A1) and (A2), partial derivatives of some quantity f transform as:

$$\bar{\partial}_j f := \frac{\partial f(\bar{\mathbf{r}}, \bar{t})}{\partial \bar{r}_j} = (\partial_i f) s_{ij} \quad (\text{A4})$$

$$\bar{\partial}_t f := \frac{\partial f(\bar{\mathbf{r}}, \bar{t})}{\partial \bar{t}} = \partial_t f + (\partial_i f) \dot{s}_{ij} \bar{r}_j, \quad (\text{A5})$$

where $\partial_i f := \partial f(\mathbf{r}, t)/\partial r_i$, $\partial_t f := \partial f(\mathbf{r}, t)/\partial t$, and $\dot{s}_{ij} := ds_{ij}/dt = ds_{ij}/d\bar{t}$. Thus, the partial time derivative in co-deforming coordinates, $\bar{\partial}_t f$, i.e. for fixed $\bar{\mathbf{r}}$, includes a term related to the box shear rate as compared to the partial time derivative with respect to lab coordinates.

3. Velocity and velocity gradient

To obtain the mapping for the velocity field, we consider a tracer particle that is perfectly advected with the flows. The velocity of that tracer particle corresponds to a total time derivative $v_i = dr_i/dt$, for which we obtain by insertion of Eq. (A1):

$$v_i = \dot{s}_{ij}\bar{r}_j + s_{ij}\bar{v}_j, \quad (\text{A6})$$

where $\bar{v}_i := d\bar{r}_i/dt = d\bar{r}_i/d\bar{t}$ is the co-deforming velocity, with $\bar{r}(\bar{t})$ being the tracer trajectory in co-deforming coordinates.

The first term in Eq. (A6) corresponds to a motion due to the affine transformation according to box coordinates. Thus, \bar{v}_i can be interpreted as the non-affine component of the flow field. This can also be seen more explicitly by computing the velocity gradient from Eq. (A6):

$$\partial_i v_j = v_{ij}^0 + s_{ij}^{-1} s_{jk} \bar{\partial}_l \bar{v}_k, \quad (\text{A7})$$

where $v_{ij}^0 := s_{ki}^{-1} \dot{s}_{jk}$ is the average box deformation rate tensor. For s_{ij} as defined in Eq. (A3), the box deformation rate tensor is:

$$v_{ij}^0 = \begin{pmatrix} \dot{l}_x/l_x & 0 \\ 0 & -\dot{l}_x/l_x \end{pmatrix} = \begin{pmatrix} \dot{L}_x/L_x & 0 \\ 0 & -\dot{L}_x/L_x \end{pmatrix}. \quad (\text{A8})$$

4. Total derivative

To obtain a transformation formula for the convective derivative, we consider again our tracer and the presence of some spatio-temporal field f . The convective derivative corresponds to the total derivative of the value of f that the tracer locally sees. Thus, we expect analogous expressions for the convective derivative in both lab and co-deforming systems, $\dot{f} := df/dt = df/d\bar{t}$. Indeed, using Eqs. (A4), (A5), and (A6), we obtain:

$$\dot{f} = \partial_t f + v_i (\partial_i f) = \bar{\partial}_t f + \bar{v}_i (\bar{\partial}_i f). \quad (\text{A9})$$

5. Fourier transform

Moreover, we define the co-deforming Fourier transformation of a quantity f such that

$$f(\bar{\mathbf{r}}) = \sum_{\bar{\mathbf{q}}} f(\bar{\mathbf{q}}) e^{i\bar{\mathbf{q}} \cdot \bar{\mathbf{r}}}, \quad (\text{A10})$$

where the sum is over all co-deforming wave vectors $\bar{\mathbf{q}} = (\bar{q}_x, \bar{q}_y)$ with $\bar{q}_i = 2\pi n_i/L_i(0)$, where $n_i \in \mathbb{Z}$ and $i \in \{x, y\}$. A co-deforming Fourier mode with wave vector $\bar{\mathbf{q}}$ is distorted over time by the overall system deformation:

$$q_x(\bar{\mathbf{q}}, t) = l_x^{-1}(t) \bar{q}_x \quad (\text{A11})$$

$$q_y(\bar{\mathbf{q}}, t) = l_x(t) \bar{q}_y. \quad (\text{A12})$$

as in Eq. (A10), we have the usual derivation rule, where the Fourier transform of $\bar{\partial}_j f(\bar{\mathbf{r}}, \bar{t})$ is $i\bar{k}_j f(\bar{\mathbf{q}}, \bar{t})$. From Eqs. (A10) and (A1) also follows that a given co-deforming Fourier mode with wave vector $\bar{\mathbf{q}}$ corresponds to a lab frame Fourier mode with wave vector \mathbf{q} with components

$$q_i = \bar{q}_j s_{ji}^{-1}, \quad (\text{A13})$$

because then we have $\bar{\mathbf{q}} \cdot \bar{\mathbf{r}} = \mathbf{q} \cdot \mathbf{r}$.

Appendix B: Dynamics in co-deforming coordinates

Using Appendix A, we can express the dimensionless dynamic equations, Eqs. (10)–(13), in co-deforming coordinates:

$$\bar{\partial}_t s + \bar{v}_i (\bar{\partial}_i s) = 0 \quad (\text{B1})$$

$$\bar{\partial}_t c + \bar{v}_i (\bar{\partial}_i c) = (D s_{ij}^{-2} \bar{\partial}_i \bar{\partial}_j - k_d) c + k_d s \quad (\text{B2})$$

$$0 = \frac{1}{4} s_{jl} \partial_i^2 \bar{v}_l - \partial_j \Pi' + \partial_i \bar{\sigma}_{ij}^a \quad (\text{B3})$$

$$s_{il} \partial_i \bar{v}_l = 0, \quad (\text{B4})$$

where $\bar{\sigma}_{ij}^a$ is given by Eq. (6). Eqs. (B3) and (B4) are still expressed using lab-frame derivatives, because this will allow for a more convenient solution of the non-affine flows in the next section.

Finally, the system size dynamics for the freely deforming system, Eq. (7), becomes:

$$\frac{dl_x}{dt} = -\text{sgn}(\alpha) l_x \iint [l_x^{-2} (\bar{\partial}_x c)^2 - l_x^2 (\bar{\partial}_y c)^2] d\bar{x} d\bar{y}, \quad (\text{B5})$$

where the integral is over the box at time point 0, i.e. the integration variables are the co-deforming coordinates \bar{x} and \bar{y} .

1. Non-affine flows

For deforming systems, we will generally consider the dynamics of source and morphogen fields in co-deforming coordinates, Eqs. (B1) and (B2). To obtain the non-affine flows, we solve Eqs. (B3) and (B4) by taking the lab-frame Fourier transform, which yields after some transformations:

$$\bar{v}_k = \frac{4i s_{ki}^{-1} q_l}{q^2} \left(\delta_{ij} - \frac{q_i q_j}{q^2} \right) \bar{\sigma}_{lj}^a \quad (\text{B6})$$

with $\bar{\sigma}_{ij}^a$ given by Eq. (6).

Note that Eq. (B6) is undefined for $\mathbf{q} = 0$. Indeed, any constant homogeneous velocity can always be added to the flow field. Here and in the following, we will ignore this, because it does not affect the physics in any way.

2. Absence of non-affine flows for $\partial_y c = 0$

If the morphogen concentration field c is homogeneous in y direction, i.e. $\partial_y c = \partial_{\bar{y}} c = 0$, then there are no non-affine flows, i.e. there are no flows in co-deforming coordinates, $\bar{\mathbf{v}} = 0$. For fixed system dimensions, this corresponds to a complete absence of flows, $\mathbf{v} = 0$.

Formally, the absence of non-affine flows follows from Eq. (B6), which links $\bar{\mathbf{v}}$ in Fourier space to the stress tensor in Fourier space. From Eq. (6) we obtain for $\partial_y c = 0$, that $\tilde{\sigma}_{xy}^a = 0$ everywhere, and $\tilde{\sigma}_{xx}^a$ is independent of y . Thus, in Fourier space, $\tilde{\sigma}_{xx}^a$ is nonzero only for wave vectors \mathbf{q} that have a vanishing y component, $q_y = 0$. Insertion in Eq. (B6) yields indeed $\bar{\mathbf{v}} = 0$.

Appendix C: Linearized dynamics

1. In co-deforming real space coordinates

We perturb the system around the dynamic state $\vec{z}_0 = (s_0(\bar{\mathbf{r}}), c_0(\bar{\mathbf{r}}), l_{x0})$ to linear order, where s_0 and c_0 only depend on \bar{x} :

$$s(\bar{\mathbf{r}}) = s_0(\bar{x}) + \delta s(\bar{\mathbf{r}}), \quad (\text{C1})$$

$$c(\bar{\mathbf{r}}) = c_0(\bar{x}) + \delta c(\bar{\mathbf{r}}), \quad (\text{C2})$$

$$l_x = l_{x0} + \delta l_x. \quad (\text{C3})$$

Because c_0 only depends on \bar{x} , we also have in the state \vec{z}_0 that $\tilde{\sigma}_{xy}^a = 0$ and there are no non-affine flows, $\bar{\mathbf{v}} = 0$ (Appendix B 2).

Combining Eqs. (C1)–(C3) with Eqs. (B1), (B2), and (B5) yields the following linearized dynamics:

$$\bar{\partial}_t \delta s = -s'_0 \delta \bar{v}_x, \quad (\text{C4})$$

$$\begin{aligned} \bar{\partial}_t \delta c = & -c'_0 \delta \bar{v}_x + k_d(\delta s - \delta c) \\ & + D s_{ij}^{-2} \bar{\partial}_i \bar{\partial}_j \delta c - 2D(\bar{\partial}_x^2 c_0) \frac{\delta l_x}{l_{x0}^3}, \end{aligned} \quad (\text{C5})$$

$$\frac{d\delta l_x(t)}{dt} = \frac{2\text{sgn}(\alpha)}{l_{x0}} \iint (\bar{\partial}_x^2 c_0) \delta c d\bar{x}d\bar{y} - \frac{dl_{x0}}{dt} \frac{\delta l_x}{l_{x0}}, \quad (\text{C6})$$

where we have introduced the notation $s'_0 := \bar{\partial}_x s_0$ and $c'_0 := \bar{\partial}_x c_0$, and we used a partial integration in the linearized l_x dynamics.

2. In co-deforming Fourier space coordinates

In co-deforming Fourier space, the linearized dynamics read:

$$\bar{\partial}_t \delta s = -s'_0 * \delta \bar{v}_x \quad (\text{C7})$$

$$\begin{aligned} \bar{\partial}_t \delta c = & -c'_0 * \delta \bar{v}_x + k_d(\delta s - \delta c) \\ & - D s_{ij}^{-2} \bar{q}_i \bar{q}_j \delta c + 2D \bar{q}_x^2 c_0 \frac{\delta l_x}{l_{x0}^3}, \end{aligned} \quad (\text{C8})$$

$$\frac{d\delta l_x(t)}{dt} = -\frac{2\text{sgn}(\alpha)}{l_{x0}} \sum_{\bar{\mathbf{q}}} \bar{q}_x^2 c_0^\dagger \delta c - \frac{dl_{x0}}{dt} \frac{\delta l_x}{l_{x0}}. \quad (\text{C9})$$

Here s'_0 and c'_0 represent the co-deforming Fourier transforms of $\bar{\partial}_x s_0$ and $\bar{\partial}_x c_0$, respectively. Furthermore, to rewrite the δl_x dynamics, we have used Parseval's identity, where the dagger, \cdot^\dagger , denotes the complex conjugate. We have moreover used the following definition of convolution operator, $*$, in co-deforming Fourier space:

$$f(\bar{\mathbf{q}}) * g(\bar{\mathbf{q}}) := \sum_{\bar{\mathbf{q}'}} f(\bar{\mathbf{q}'}) g(\bar{\mathbf{q}} - \bar{\mathbf{q}'}), \quad (\text{C10})$$

where the sum is over all co-deforming wave vectors $\bar{\mathbf{q}}' = (\bar{q}'_x, \bar{q}'_y)$ with $\bar{q}'_i = 2\pi n'_i / L_i(0)$, where $n'_i \in \mathbb{Z}$ and $i \in \{x, y\}$. For a fixed system size, we ignore the δl_x dynamics and the δl_x term in the δc dynamics.

To close Eqs. (C7)–(C9), we still need to insert the x -component of non-affine flow field perturbation, $\delta \bar{v}_x$. For convenience, we will use *lab-frame* Fourier modes to compute $\delta \bar{v}_x$. Specifically, we use Eq. (B6), which expresses $\bar{\mathbf{v}}$ in terms of the active stress tensor $\tilde{\sigma}_{ij}^a$. We obtain to linear order:

$$\delta \bar{v}_x(q, \phi) = \frac{4i \sin \phi}{ql_{x0}} \left[\sin 2\phi \delta \tilde{\sigma}_{xx}^a - \cos 2\phi \delta \tilde{\sigma}_{xy}^a \right], \quad (\text{C11})$$

where q and ϕ denote the amplitude and orientation, respectively, of the lab-frame wave vector $\mathbf{q} = q(\cos \phi, \sin \phi)$.

We further express $\delta \tilde{\sigma}_{ij}^a$ in terms of δc using Eq. (6). To linear order, in lab-frame Fourier space:

$$\delta \tilde{\sigma}_{xj}^a = \frac{i \text{sgn}(\alpha)}{l_{x0}} c'_0 * (q_j \delta c) \quad \text{for } j \in \{x, y\}. \quad (\text{C12})$$

The other two components of the symmetric traceless tensor $\delta \tilde{\sigma}_{ij}^a$ are obtained through the relations $\delta \tilde{\sigma}_{yy}^a = -\delta \tilde{\sigma}_{xx}^a$ and $\delta \tilde{\sigma}_{yx}^a = \delta \tilde{\sigma}_{xy}^a$. The convolution operator in lab-frame Fourier coordinates in Eq. (C12) is defined analogously to Eq. (C10) as:

$$f(\mathbf{q}) * g(\mathbf{q}) := \sum_{\mathbf{q}'} f(\mathbf{q}') g(\mathbf{q} - \mathbf{q}'), \quad (\text{C13})$$

where the sum is over all lab-frame wave vectors $\mathbf{q}' = (q'_x, q'_y)$ with $q'_i = 2\pi n'_i / L_i(t)$, where $n'_i \in \mathbb{Z}$ and $i \in \{x, y\}$.

Combining (C11) and (C12), we obtain:

$$\begin{aligned} \delta \bar{v}_x = & -\frac{4\text{sgn}(\alpha) \sin \phi}{ql_{x0}^2} \left\{ \sin 2\phi \left[c'_0 * (q_x \delta c) \right] \right. \\ & \left. - \cos 2\phi \left[c'_0 * (q_y \delta c) \right] \right\}. \end{aligned} \quad (\text{C14})$$

The system of equations, Eqs. (C7)–(C9), and (C14), is now closed.

3. Numerical solution

In the special case of a linear source profile, we can solve the linearized dynamics analytically, because the

gradients of s_0 and c_0 are constant, and thus the convolutions in Eqs. (C7), (C8), and (C14) collapse to a simple scaling factor. However, in general this is not the case, and we need to solve the linearized dynamics numerically.

To numerically compute the convolutions in Eqs. (C7), (C8), and (C14), we need to take into account that the numerical real-space representations of our fields are spatially discretized. To discuss the main ideas, we will discuss here the case of a single spatial dimension, \bar{x} , in co-deforming coordinates. The generalization to lab frame coordinates and/or several dimensions will be straight forward. Specifically, we consider the periodic interval $\bar{x} \in [-L_x(0)/2, +L_x(0)/2]$ to be discretized by N_x equal-length steps $\Delta\bar{x} = L_x(0)/N_x$, where N_x is an even integer. Any function $f(\bar{x})$ is represented by a set of numbers f_k with $k = -N_x/2, -N_x/2+1, \dots, 0, \dots, N_x/2-1$, such that $f_k = f(k\Delta\bar{x})$. As a consequence, the Fourier series are not infinite any more as in Eq. (A10), but instead cut off at some finite wave vectors. In particular, the numerical co-deforming Fourier transform of f is represented by a set of complex numbers \tilde{f}_j with $j = -N_x/2, -N_x/2+1, \dots, 0, \dots, N_x/2-1$, where $\tilde{f}_j = f(\bar{q}_x = j\bar{q}_0)$ with $\bar{q}_0 := 2\pi/L_x(0)$. Eq. (A10) then becomes:

$$f_k = \sum_{j=-N_x/2}^{N_x/2-1} \tilde{f}_j e^{2\pi i(jk/N_x)}, \quad (\text{C15})$$

where we used that $\bar{q}_0\Delta\bar{x} = 2\pi/N_x$. To maintain in this discretized space the property that the Fourier transform of the product of two functions f and g is the convolution of their respective Fourier transforms,

$$(\widetilde{fg})_j = (\tilde{f} * \tilde{g})_j, \quad (\text{C16})$$

we need to define the following discrete convolution operator:

$$(\tilde{f} * \tilde{g})_j = \sum_{j'=-N_x/2}^{N_x/2-1} \tilde{f}_{j'} \tilde{g}_{j-j'} \quad (\text{C17})$$

for $j = -N_x/2, -N_x/2+1, \dots, 0, \dots, N_x/2-1$. Yet, we see that the index $j-j'$ of \tilde{g} can get outside of the range $-N_x/2, -N_x/2+1, \dots, N_x/2-1$. For Eq. (C16) to still be fulfilled, we need to define \tilde{g} to be periodic, such that $\tilde{g}_{(j+nN_x)} := \tilde{g}_j$ for all $n \in \mathbb{Z}$. In this sense, the convolution in Fourier space of our discretized function is *circular*. We use such a circular definition to numerically compute the convolutions in Eqs. (C7), (C8), and (C14), to preserve the relation Eq. (C16).

To numerically solve the linearized dynamics, Eqs. (C7)–(C9), we use an exponential Ansatz for the time dependence of the perturbations,

$$\delta s(\bar{\mathbf{q}}, t) = \delta \hat{s}(\bar{\mathbf{q}}) e^{\omega t} \quad (\text{C18})$$

$$\delta c(\bar{\mathbf{q}}, t) = \delta \hat{c}(\bar{\mathbf{q}}) e^{\omega t} \quad (\text{C19})$$

$$\delta l_x(t) = \delta \hat{l}_x e^{\omega t}. \quad (\text{C20})$$

Inserting this in Eqs. (C7)–(C9) yields an eigenvalue problem:

$$\omega \delta \hat{\mathbf{z}} = M \cdot \delta \hat{\mathbf{z}}, \quad (\text{C21})$$

where the components of $\delta \hat{\mathbf{z}}$ are $\delta \hat{l}_x$ and the values of $\delta \hat{s}(\bar{\mathbf{q}})$ and $\delta \hat{c}(\bar{\mathbf{q}})$ for all $N_x N_y$ discrete values of the co-deforming wave vector $\bar{\mathbf{q}}$. Thus, $\delta \hat{\mathbf{z}}$ has $2N_x N_y + 1$ components. The matrix M usually couples not only $\delta \hat{s}$ and $\delta \hat{c}$ components for the same wave vector $\bar{\mathbf{q}}$ to each other, but due to the convolutions in Eqs. (C7), (C8), and (C14), there is also mixing occurring across different wave vectors.

Appendix D: Fixed-size system with linear source

For a linear source and morphogen fields, the active flows, Eq. (C14), simplify to:

$$\delta v_x = -\omega_{\text{act}} \delta c \quad \text{with } \omega_{\text{act}} = 4 \text{sgn}(\alpha) \sin^2 \phi, \quad (\text{D1})$$

where ω_{act} is the perturbation growth rate for the case of a boundary-provided gradient without source field [32]. With this, the linearized dynamics, Eqs. (C7)–(C8) become:

$$\partial_t \delta s = \omega_{\text{act}} \delta c, \quad (\text{D2})$$

$$\partial_t \delta c = [\omega_{\text{act}} - Dq^2 - k_d] \delta c + k_d \delta s. \quad (\text{D3})$$

Thus, the convolutions in Eqs. (C7), (C8), and (C14) collapse to a constant prefactor. As a consequence, the solutions of the system are Fourier modes. In the following, we first discuss the limiting case of no diffusion before presenting the general solution.

1. No diffusion, $D = 0$

To solve the eigenvalue problem in this case, we define

$$\delta \Delta = \delta c - \delta s \quad (\text{D4})$$

$$\delta b = \delta c + \frac{k_d}{\omega_{\text{act}}} \delta s. \quad (\text{D5})$$

Inserting this into Eqs. (D2) and (D3), we obtain:

$$\partial_t \delta \Delta = -k_d \delta \Delta \quad (\text{D6})$$

$$\partial_t \delta b = \omega_{\text{act}} \partial_t \delta b. \quad (\text{D7})$$

Hence, the difference between both morphogen and source, $\delta \Delta$, decays at rate k_d , while a superposition of both, δb , grows with the same growth rate as the system without source [32].

2. General case

With an exponential Ansatz, where $\delta s \sim \delta c \sim e^{\omega t}$, we obtain an eigenvalue problem, whose solutions in ω are:

$$\omega_{\pm} = \frac{1}{2} \left[\mathcal{T} \pm \sqrt{\mathcal{T}^2 + 4k_d \omega_{\text{act}}} \right], \quad (\text{D8})$$

where $\mathcal{T} = \omega_{\text{act}} - Dq^2 - k_d$. The corresponding eigenvectors in $(\delta s, \delta c)$ are

$$\mathbf{v}_+ = \begin{pmatrix} \omega_+ \\ \omega_{\text{act}} \end{pmatrix} \quad \text{and} \quad \mathbf{v}_- = \begin{pmatrix} \omega_- \\ \omega_{\text{act}} \end{pmatrix}, \quad (\text{D9})$$

respectively.

Appendix E: Fixed-size system with localized source

1. Value of s_b in dimensionless units

As we discussed in [section II C](#), we set the value of s_b such that the magnitude of the deformation rate of a system with $L_x = L_y = 1$ is one. This means that we set

$$s_b = \left[\sum_{q_x} \frac{k_d^2 |m(q_x)|^2}{(k_d + Dq_x^2)^2} \right]^{-1/2} \quad (\text{E1})$$

where $m(q_x)$ is the Fourier transform of the function

$$m(x) = \exp \left(\frac{\cos(q_0 x)}{(q_0 w)^2} \right) \quad (\text{E2})$$

which is defined on the interval $x \in [-1/2, 1/2)$, and where $q_0 = 2\pi/L_x$. Indeed, using Eqs. (7) and (21), one obtains that with the value of s_b from Eq. (E1), a von Mises source profile, Eq. (20), and $L_x = L_y = 1$, the absolute value of the shear rate is one.

2. Numerically growing modes in gradient-extensile systems

In [section IV](#), we found that in a gradient-extensile systems, some modes showed a positive growth rate. Yet, when we increased the spatial discretization N_x , the value of the growth rate decreased as a power law with N_x ([Figure 3H](#)), suggesting that these positive growth rates may just be a numerical artifact. Here we discuss this question further.

We discuss the positive growth rates for the limit $w \rightarrow \infty$, for which the source profile $s_0(\mathbf{r})$, defined in Eq. (20), becomes a cosine. We obtained the modes with positive growth rates, using the approach described in [Appendix C 3](#). Yet, for this we used the circular convolutions, Eq. (C17), which in a way is a natural choice, imposed by the fact that we do not have infinitely fine resolution of $s(x)$ and $c(x)$, which would allow to have the

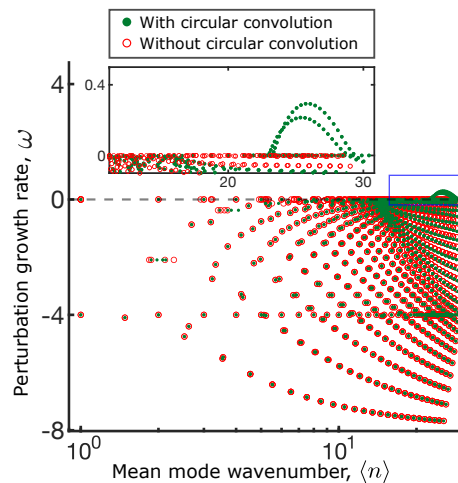


FIG. 8. Linear stability of gradient-extensile systems with $w \rightarrow \infty$, i.e., where the source profile converges to a single cosine mode. Green dots and green circles represent the numerical analysis with and without discrete periodic convolution, respectively. Inset showing that perturbation modes with $\omega > 0$ disappear when convolution is not periodic.

information about these fields at arbitrarily large wave number \mathbf{q} . Instead, because these fields are discretized, the Fourier amplitude at high wave vectors just become periodic, as described in [Appendix C 3](#). In other words, due to a limited resolution, we do not know what the amplitude for high wave vectors is and we “just” set them to some values assuming periodicity. One could also use a different approach, by assuming that the Fourier amplitudes at these high wave vectors just vanishes. This corresponds to an alternative numerical implementation of the Fourier-space convolution. Specifically, we replace the circular convolutions by “non-circular” convolutions where we ignore the periodicity of the discrete Fourier transforms, i.e., we replace Eq. (C17) by:

$$(\tilde{f} * \tilde{g})_j = \sum_{j'=-N_x/2}^{N_x/2-1} \tilde{f}_{j'} \tilde{g}_{j-j'} \Theta_{j-j'} \quad (\text{E3})$$

where

$$\Theta_k = \begin{cases} 1 & \text{for } -N_x/2 \leq k \leq N_x/2 - 1, \\ 0 & \text{otherwise.} \end{cases} \quad (\text{E4})$$

The factor $\Theta_{j-j'}$ explicitly ensures that there is any periodicity in $\tilde{g}_{j-j'}$ is ignored. We compare the solutions of the eigenvalue problem, Eq. (C21), between circular and non-circular convolution in [Figure 8](#), and we find that while most of the modes did not change much, the modes with positive growth rates disappeared when using the non-circular convolutions. This further suggests that these positive growth rates are merely an artifact of our spatial discretization.

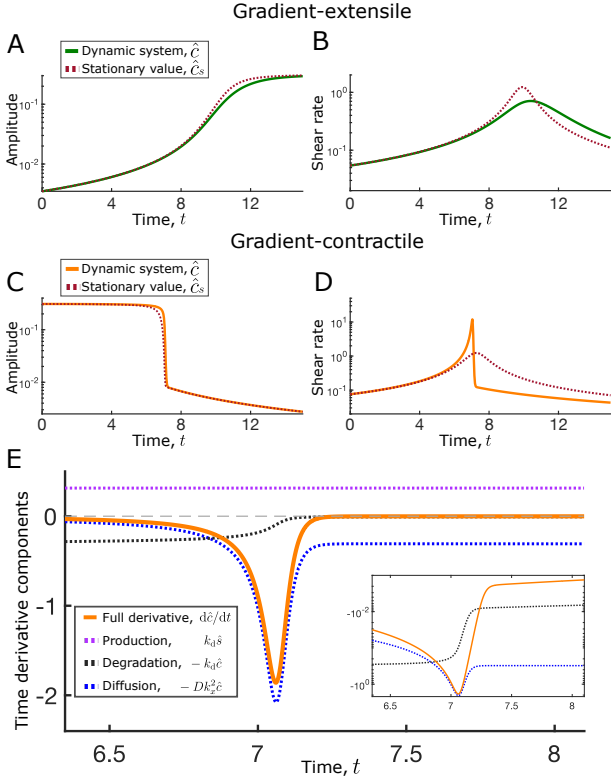


FIG. 9. System dynamics of a freely deforming system with a diffusive morphogen, $\tilde{v}_{xx}^0 = \tilde{v}_{xx}^{\text{free}}, D = 10^{-2}$. (A) Morphogen magnitude over time for the gradient-extensile case, where we compare the dynamic system (green) with the stationary value (Eq. (F3), dashed red) as a function of time (B) Absolute values of shear rates of the systems in panel A. (C,D) Morphogen and shear rate magnitudes for the gradient-contractile case. (E) Decomposition of the partial time derivative of the dynamic morphogen amplitude in the gradient-contractile case (see text).

Appendix F: Deforming system with localized source

1. Discussion of the system size dynamics

Starting with a gradient-extensile system with dimension $L_x = 1/15$, we observe that the aspect ratio increases over time as expected (green curve in Figure 7A). However, the shear rate first increases and then decreases (green curve in Figure 7B), in contrast to the case without diffusion, where it monotonically decreases (Figure 6B). To understand this behavior, we first note that without any non-affine flows (i.e. $\bar{\mathbf{v}} = \mathbf{0}$), both morphogen and source profiles keep their cosine profiles, $s(\mathbf{r}, t) = \hat{s}[\cos(2\pi x/L_x) + 1]$ and $c(\mathbf{r}, t) = \hat{c}(t) \cos(2\pi x/L_x) + c_{\text{offset}}(t)$, while only the morphogen amplitude $\hat{c}(t)$ and offset $c_{\text{offset}}(t)$ vary over time. Without non-affine flows we can thus simplify the system dy-

namics to:

$$\frac{d\hat{c}}{dt} = -k_d(\hat{c} - \hat{s}) - 4\pi^2 D \frac{\hat{c}}{L_x^2} \quad (\text{F1})$$

$$\frac{dL_x}{dt} = -\frac{2\pi^2 \text{sgn}(\alpha) \hat{c}^2}{L_x}, \quad (\text{F2})$$

where the offset $c_{\text{offset}}(t)$ does not matter for the system size dynamics. We also noted that at each time point the morphogen amplitude \hat{c} is relatively well approximated by its stationary value \hat{c}_s for given L_x (Figure 9A). This corresponds to the adiabatic limit where the c dynamics is fast as compared to the L_x dynamics. This stationary value \hat{c}_s is given by Eq. (F1) for $d\hat{c}/dt = 0$, which implies:

$$\hat{c}_s = \left[1 + \frac{4\pi^2 D}{k_d L_x^2} \right]^{-1} \hat{s}. \quad (\text{F3})$$

Indeed, when numerically solving the system size dynamics given by Eq. (F2) with the stationary solution for \hat{c}_s , Eq. (F3) instead of the actual \hat{c} dynamics, Eq. (F1), we get a similar behavior (Figure 9B). This behavior can be readily explained as initially L_x is small, and thus the diffusion term in \hat{c} dominates, such that $\hat{c}_s \sim L_x^2$. Inserting this into Eq. (F2) gives a shear rate scaling of $(dL_x/dt)/L_x \sim L_x^2$, which leads for a gradient-extensile system ($\text{sgn}(\alpha) = -1$) to an accelerating pure shear. Intuitively, this is because for small L_x , diffusion dominates, which generally lowers the amplitude of the morphogen field. In this limit, increasing L_x decreases diffusion and thus increases the morphogen amplitude and, as a consequence, the shear rate. However, as soon as L_x becomes large enough, the diffusion term in Eq. (F3) can be neglected, and we have almost constant \hat{c} , such that the shear rate scales as $(dL_x/dt)/L_x \sim L_x^{-2}$. Hence, the shear decelerates over time due to the expansion of the morphogen field (section V A).

For gradient-contractile systems, we observe a much more erratic system size behavior. The orange curves in Figure 7A,B show example trajectories for a system with initially $L_x = 5$. In particular, the shear rate shows a transient, but pronounced peak before quickly switching to much slower dynamics (Figure 7B inset). This behavior can be quantitatively understood in terms of three distinct phases. In a first phase, L_x is large, such that the diffusion term can be neglected in the morphogen dynamics, so that, according to Eq. (F1), \hat{c} keeps its initial value of approximately \hat{s} . Thus, according to Eq. (F2), the shear rate initially scales as $(dL_x/dt)/L_x \sim -L_x^{-2}$, leading to a decrease in L_x and an increase in the shear rate, as in the case without diffusion (section V A). The second phase starts when L_x becomes small enough for the diffusion term to dominate in the \hat{c} dynamics, Eq. (F1), such that $d\hat{c}/dt = -4\pi^2 D \hat{c}/L_x^2$ (Figure 9E). Dividing Eq. (F2) by $d\hat{c}/dt$, we get $dL_x/d\hat{c} = \text{sgn}(\alpha) \hat{c} L_x / 2D$, which implies that $L_x \sim \exp[\text{sgn}(\alpha) \hat{c}^2 / 4D]$. This limit corresponds to the transient peak in the shear rate (Figure 9C,D). During this transient phase, \hat{c} is rapidly decreasing, while for very small \hat{c} the system dimension

$L_x \sim \exp[\text{sgn}(\alpha)\hat{c}^2/4D]$ varies only little as compared to \hat{c} . Thus, as \hat{c} decreases, the diffusion term in Eq. (F1) at some point becomes smaller than the source term $k_d\hat{s}$, at which point this transient stops. During the subsequent third phase, the shear rate becomes small due to the small \hat{c} , which allows the morphogen dynamics to be close to its stationary state. But since L_x is also small, the diffusion term still dominates in Eq. (F3), and so the morphogen amplitude scales as $\hat{c} \sim L_x^2$, such that the shear rate scales as $(dL_x/dt)/L_x \sim L_x^2$, and thus slows down over time. Taken together, while the shear rate varies for both, gradient-extensile and gradient-contractile systems, its behavior is much more erratic in the gradient-contractile case.

2. Affine diffusion-shear instability

To discuss the affine diffusion-shear instability, we start from the linearized dynamics in Fourier space, Eqs. (C7)–(C9), where we set non-affine flows to zero, $\delta\bar{\mathbf{v}} = 0$, we ignore any variations of the source field, $\delta s = 0$, and we ignore any y -dependence of the perturbations. We obtain from Eqs. (C8) and (C9) with an exponential Ansatz for the time dependency, $\delta c(\bar{q}_x, t) = \delta\tilde{c}(\bar{q}_x)e^{\omega t}$ and $\delta l_x(t) = \delta\tilde{l}_x e^{\omega t}$:

$$\omega\delta\tilde{c}(\bar{q}_x) = -k_d(1 + \lambda^2 q_x^2)\delta\tilde{c}(\bar{q}_x) + 2k_d\lambda^2 q_x^2 c_0(\bar{q}_x) \frac{\delta\tilde{l}_x}{l_x} \quad (\text{F4})$$

$$\omega \frac{\delta\tilde{l}_x}{l_x} = -2\text{sgn}(\alpha) \sum_{\bar{q}_x} q_x^2 c_0^\dagger(\bar{q}_x) \delta\tilde{c}(\bar{q}_x) + \text{sgn}(\alpha) \frac{\delta\tilde{l}_x}{l_x} \sum_{\bar{q}_x} q_x^2 |c_0(\bar{q}_x)|^2. \quad (\text{F5})$$

Here, we also substituted the diffusion length scale $\lambda = \sqrt{D/k_d}$ and the lab-frame wave vector $q_x = \bar{q}_x/l_x$. If this linear system of equations has a positive eigenvalue ω , then there is an instability.

a. Cosine source profile

For the case of a cosine profile, the only nonzero values of $c_0(\bar{q}_x)$ are $c_0 \equiv c_0(\pm\bar{q}_0)$ with $\bar{q}_0 = 2\pi/L_x(0)$. Then, Eqs. (F4) and (F5) become:

$$\omega\delta\tilde{c} = -k_d(1 + \lambda^2 q_0^2)\delta\tilde{c} + 2k_d\lambda^2 q_0^2 c_0 \frac{\delta\tilde{l}_x}{l_x} \quad (\text{F6})$$

$$\omega \frac{\delta\tilde{l}_x}{l_x} = -4\text{sgn}(\alpha)q_0^2 c_0^\dagger \delta\tilde{c} + 2\text{sgn}(\alpha)q_0^2 |c_0|^2 \frac{\delta\tilde{l}_x}{l_x}, \quad (\text{F7})$$

where $q_0(t) := \bar{q}_0/l_x(t) = 2\pi/L_x(t)$. There are two eigenvalues, ω_1 and ω_2 with $\omega_1 \leq \omega_2$, and the larger eigenvalue is given by: The larger of the two eigenvalues is:

$$\omega_2 = \frac{1}{2} \left[\mathcal{T} + \sqrt{\mathcal{T}^2 - 4\mathcal{D}} \right], \quad (\text{F8})$$

where $\mathcal{T} := -k_d(1 + \lambda^2 q_0^2) + 2\text{sgn}(\alpha)q_0^2 |c_0|^2$ and $\mathcal{D} := -2\text{sgn}(\alpha)k_d q_0^2 |c_0|^2 (1 - 3\lambda^2 q_0^2)$ are trace and determinant, respectively, of the matrix on the right-hand side of Eqs. (F6) and (F7).

In the gradient-extensile case, $\text{sgn}(\alpha) = -1$, we have that $\omega_1 + \omega_2 = \mathcal{T} < 0$. Thus, at least one eigenvalue is negative. The product of both eigenvalues is given by $\omega_1\omega_2 = \mathcal{D} = 2k_d q_0^2 |c_0|^2 (1 - 3\lambda^2 q_0^2)$. Hence, there is a positive eigenvalue iff $3\lambda^2 q_0^2 > 1$, i.e. iff $2\pi\lambda\sqrt{3} > L_x$.

b. Arbitrary source profile

For the case of an arbitrary source profile s_0 , we focus on the gradient-extensile case, $\text{sgn}(\alpha) = -1$. We discuss the existence of positive solutions ω by first expressing $\delta\tilde{c}(\bar{q}_x)$ in terms of $\delta\tilde{l}_x$ and ω using Eq. (F4):

$$\delta\tilde{c}(\bar{q}_x) = \frac{2\lambda^2 q_x^2 c_0(\bar{q}_x)}{1 + \omega/k_d + \lambda^2 q_x^2} \frac{\delta\tilde{l}_x}{l_x}. \quad (\text{F9})$$

Insertion into Eq. (F5) yields:

$$\begin{aligned} \omega &= \sum_{\bar{q}_x} q_x^2 |c_0(\bar{q}_x)|^2 \frac{4\lambda^2 q_x^2}{1 + \omega/k_d + \lambda^2 q_x^2} - \sum_{\bar{q}_x} q_x^2 |c_0(\bar{q}_x)|^2 \\ &= \sum_{\bar{q}_x} q_x^2 |c_0(\bar{q}_x)|^2 \frac{3\lambda^2 q_x^2 - 1 - \omega/k_d}{1 + \omega/k_d + \lambda^2 q_x^2}. \end{aligned} \quad (\text{F10})$$

To solving this self-consistent equation for ω , we look for the zeros of the function

$$f_\lambda(\omega) := -\omega + \sum_{\bar{q}_x} q_x^2 |c_0(\bar{q}_x)|^2 \frac{3\lambda^2 q_x^2 - 1 - \omega/k_d}{1 + \omega/k_d + \lambda^2 q_x^2}. \quad (\text{F11})$$

Specifically, we now show that iff $f_\lambda(0) > 0$, there exists a positive solution in ω , i.e. an $\omega > 0$ for which $f_\lambda(\omega) = 0$. This means that there is an affine diffusion-shear instability iff $f_\lambda(0) > 0$. To show this, we first assume that there is an $\omega > 0$ for which $f_\lambda(\omega) = 0$. Then, we have:

$$\begin{aligned} 0 &< \omega \\ &= \sum_{\bar{q}_x} q_x^2 |c_0(\bar{q}_x)|^2 \frac{3\lambda^2 q_x^2 - 1 - \omega/k_d}{1 + \omega/k_d + \lambda^2 q_x^2} \\ &< \sum_{\bar{q}_x} q_x^2 |c_0(\bar{q}_x)|^2 \frac{3\lambda^2 q_x^2 - 1}{1 + \lambda^2 q_x^2} \\ &= f_\lambda(0). \end{aligned} \quad (\text{F12})$$

In these transformations, we have subsequently used $\omega > 0$, $f_\lambda(\omega) = 0$, $\omega > 0$, and the definition of $f_\lambda(\omega)$. Thus, if there is an $\omega > 0$ for which $f_\lambda(\omega) = 0$, then $f_\lambda(0) > 0$.

Second, we assume that $f_\lambda(0) > 0$. To show that there is a positive zero of f_λ , we need to show that there is a positive $\hat{\omega} > 0$ for which $f_\lambda(\hat{\omega}) < 0$. Then, the Zwischenwertsatz implies that there is an ω with $0 < \omega < \hat{\omega}$ such

that $f_\lambda(\omega) = 0$. Indeed, for $\hat{\omega} = 3 \sum_{\bar{q}_x} q_x^2 |c_0(\bar{q}_x)|^2$, we find that:

$$\begin{aligned} f_\lambda(\hat{\omega}) &= -3 \sum_{\bar{q}_x} q_x^2 |c_0(\bar{q}_x)|^2 \\ &\quad + \sum_{\bar{q}_x} q_x^2 |c_0(\bar{q}_x)|^2 \frac{3\lambda^2 q_x^2 - 1 - \hat{\omega}/k_d}{1 + \hat{\omega}/k_d + \lambda^2 q_x^2} \\ &= \sum_{\bar{q}_x} q_x^2 |c_0(\bar{q}_x)|^2 \frac{-2(1 + \hat{\omega}/k_d)}{1 + \hat{\omega}/k_d + \lambda^2 q_x^2} \\ &< 0. \end{aligned} \tag{F13}$$

Thus, if $f_\lambda(0) > 0$ then f_λ has a positive zero and the affine diffusion-shear instability exists. Taken together,

the sign of $f_\lambda(0)$ directly indicates the existence of an instability.

Finally, we discuss the sign of $f_\lambda(0)$. Using Eq. (21), we can express $f_\lambda(0)$ in terms of the source profile:

$$f_\lambda(0) = \frac{1}{\lambda^2} \sum_{\bar{q}_x} |s_0(\bar{q}_x)|^2 \frac{\lambda^2 q_x^2 (3\lambda^2 q_x^2 - 1)}{(1 + \lambda^2 q_x^2)^3}. \tag{F14}$$

Choosing for s_0 the von Mises profile in Eq. (20) with finite width w , we numerically obtain $f_\lambda(0) > 0$ iff $\lambda > gw$ with $g \approx 0.639$ in the limit where $w \ll L_x$ (i.e. where the von Mises profile becomes a Gaussian with standard deviation w). However, the precise value of g depends on the shape of the profile s_0 . For a rectangular profile of s_0 , we numerically even found that the instability always occurs.

-
- [1] L. Wolpert, C. Tickle, and A. M. Arias, *Principles of Development* (Oxford University Press, 2015).
- [2] J. A. Zallen and E. Wieschaus, Patterned Gene Expression Directs Bipolar Planar Polarity in *Drosophila*, *Dev. Cell* **6**, 343 (2004).
- [3] B. Bénazéraf, P. Francois, R. E. Baker, N. Denans, C. D. Little, and O. Pourquie, A random cell motility gradient downstream of FGF controls elongation of an amniote embryo, *Nature* **466**, 248 (2010).
- [4] A. Shindo, Models of convergent extension during morphogenesis, Wiley Interdisciplinary Reviews: Developmental Biology **7**, 10.1002/wdev.293 (2018).
- [5] K. A. Johansen, D. D. Iwaki, and J. A. Lengyel, Localized JAK/STAT signaling is required for oriented cell rearrangement in a tubular epithelium, *Development* **130**, 135 (2003).
- [6] C. M. Karner, R. Chirumamilla, S. Aoki, P. Igarashi, J. B. Wallingford, and T. J. Carroll, Wnt9b signaling regulates planar cell polarity and kidney tubule morphogenesis, *Nature Genetics* **41**, 793 (2009).
- [7] A. Saxena, B. Denholm, S. Bunt, M. Bischoff, K. VijayRaghavan, and H. Skaer, Epidermal Growth Factor Signalling Controls Myosin II Planar Polarity to Orchestrate Convergent Extension Movements during *Drosophila* Tubulogenesis, *PLoS Biology* **12**, 1002013 (2014).
- [8] R. Etournay, M. Popović, M. Merkel, A. Nandi, C. Blasse, B. Aigouy, H. Brandl, G. Myers, G. Salbreux, F. Jülicher, and S. Eaton, Interplay of cell dynamics and epithelial tension during morphogenesis of the *Drosophila* pupal wing, *Elife* **4**, e07090 (2015).
- [9] S. Hopyan, Biophysical regulation of early limb bud morphogenesis, *Developmental Biology* **429**, 429 (2017).
- [10] H. Tao, M. Zhu, K. Lau, O. K. W. Whitley, M. Samani, X. Xiao, X. X. Chen, N. A. Hahn, W. Liu, M. Valencia, M. Wu, X. Wang, K. D. Felon, C. C. Pasiliao, D. Hu, J. Wu, S. Spring, J. Ferguson, E. P. Karuna, R. M. Henkelman, A. Dunn, H. Huang, H.-Y. H. Ho, R. Atit, S. Goyal, Y. Sun, and S. Hopyan, Oscillatory cortical forces promote three dimensional cell intercalations that shape the murine mandibular arch, *Nature Communications* **10**, 1703 (2019).
- [11] C. Bertet, L. Sulak, and T. Lecuit, Myosin-dependent junction remodelling controls planar cell intercalation and axis elongation, *Nature* **429**, 667 (2004).
- [12] F. Bosveld, I. Bonnet, B. Guirao, S. Tlili, Z. Wang, A. Petailot, R. Marchand, P.-L. Bardet, P. Marcq, F. Graner, and Y. Bellaiche, Mechanical Control of Morphogenesis by Fat/Dachsous/Four-Jointed Planar Cell Polarity Pathway, *Science* (80-.) **336**, 724 (2012).
- [13] C. Collinet, M. Rauzi, P. F. Lenne, and T. Lecuit, Local and tissue-scale forces drive oriented junction growth during tissue extension, *Nature Cell Biology* **17**, 1247 (2015).
- [14] M. Behrndt, G. Salbreux, P. Campinho, R. Hauschild, F. Oswald, J. Roensch, S. W. Grill, and C. P. Heisenberg, Forces driving epithelial spreading in zebrafish gastrulation, *Science* **338**, 257 (2012).
- [15] S. J. Streichan, M. Lefebvre, N. Noll, E. F. Wieschaus, and B. I. Shraiman, Global morphogenetic flow is accurately predicted by the spatial distribution of myosin motors, *eLife* **7**, e27454 (2018).
- [16] A. Stokkermans, A. Chakrabarti, K. Subramanian, L. Wang, S. Yin, P. Moghe, P. Steenbergen, G. Mönke, T. Hiiragi, R. Prevedel, L. Mahadevan, and A. Ikmi, Muscular hydraulics drive larva-polyp morphogenesis, *Current Biology* **32**, 4707 (2022).
- [17] E. W. Gehrels, B. Chakraborty, M.-E. Perrin, M. Merkel, and T. Lecuit, Curvature gradient drives polarized tissue flow in the *Drosophila* embryo, *Proceedings of the National Academy of Sciences* **120**, e2214205120 (2023).
- [18] N. A. Dye, M. Popovic, K. V. Iyer, J. F. Fuhrmann, R. Piscitello-Gómez, S. Eaton, and F. Jülicher, Self-organized patterning of cell morphology via mechanosensitive feedback, *eLife* **10**, 10.7554/ELIFE.57964 (2021).
- [19] M. Serra, G. S. Nájera, M. Chuai, A. M. Plum, S. Santhosh, V. Spandan, C. J. Weijer, and L. Mahadevan, A mechanochemical model recapitulates distinct vertebrate gastrulation modes, *Science advances* **9**, eadh8152 (2023).
- [20] S. Gsell, S. Tlili, M. Merkel, and P.-F. Lenne, Marangoni-like tissue flows enhance symmetry breaking of embryonic organoids, *bioRxiv* 10.1101/2023.09.22.559003 (2024).
- [21] K. Barrett, S. Anand, V. Thome, P.-F. Lenne, and

- M. Merkel, Epithelial-mesenchymal boundary guides cell shapes and axis elongation in embryonic explants, *bioRxiv* [10.1101/2024.08.20.608779](https://doi.org/10.1101/2024.08.20.608779) (2024).
- [22] N. H. Claussen, F. Brauns, and B. I. Shraiman, A geometric-tension-dynamics model of epithelial convergent extension, *Proceedings of the National Academy of Sciences* **121**, e2321928121 (2024), <https://www.pnas.org/doi/pdf/10.1073/pnas.2321928121>.
- [23] A. Ioratim-Uba, T. B. Liverpool, and S. Henkes, Mechanochemical active feedback generates convergence extension in epithelial tissue, *Physical Review Letters* **131**, 238301 (2023).
- [24] R. A. Simha and S. Ramaswamy, Hydrodynamic fluctuations and instabilities in ordered suspensions of self-propelled particles, *Phys. Rev. Lett.* **89**, 058101 (2002), [arXiv:0108301v2 \[arXiv:cond-mat\]](https://arxiv.org/abs/0108301v2).
- [25] R. Voituriez, J. F. Joanny, and J. Prost, Spontaneous flow transition in active polar gels, *Europhys. Lett.* **70**, 404 (2005), [arXiv:0503022 \[q-bio\]](https://arxiv.org/abs/0503022).
- [26] M. C. Marchetti, J. F. Joanny, S. Ramaswamy, T. B. Liverpool, J. Prost, M. Rao, and R. A. Simha, Hydrodynamics of soft active matter, *Reviews of Modern Physics* **85**, 1143 (2013), [arXiv:1207.2929v1](https://arxiv.org/abs/1207.2929v1).
- [27] S. von der Hardt, J. Bakkers, A. Inbal, L. Carvalho, L. Solnica-Krezel, C. P. Heisenberg, and M. Hammer-smidt, The Bmp Gradient of the Zebrafish Gastrula Guides Migrating Lateral Cells by Regulating Cell-Cell Adhesion, *Current Biology* **17**, 475 (2007).
- [28] G. Tkačik, J. O. Dubuis, M. D. Petkova, and T. Gregor, Positional Information, Positional Error, and Readout Precision in Morphogenesis: A Mathematical Framework, *Genetics* **199**, 39 (2015), [arXiv:1404.5599](https://arxiv.org/abs/1404.5599).
- [29] H. Ninomiya, R. P. Elinson, and R. Winklbauer, Anteroposterior tissue polarity links mesoderm convergent extension to axial patterning, *Nature* **430**, 364 (2004).
- [30] J. Lavalou, Q. Mao, S. Harmansa, S. Kerridge, A. C. Lellouch, J. M. Philippe, S. Audebert, L. Camoin, and T. Lecuit, Formation of polarized contractile interfaces by self-organized Toll-8/Cir1 GPCR asymmetry, *Dev. Cell* **56**, 1574 (2021).
- [31] Z. Wang, M. C. Marchetti, and F. Brauns, Patterning of morphogenetic anisotropy fields, *Proceedings of the National Academy of Sciences of the United States of America* **120**, e2220167120 (2023), [arXiv:2212.12215](https://arxiv.org/abs/2212.12215).
- [32] M. Ibrahimi and M. Merkel, Deforming polar active matter in a scalar field gradient, *New Journal of Physics* **25**, 013022 (2023), [arXiv:2206.12850](https://arxiv.org/abs/2206.12850).
- [33] O. Wartlick, P. Mumcu, A. Kicheva, T. Bittig, C. Seum, F. Jülicher, and M. González-Gaitán, Dynamics of Dpp signaling and proliferation control, *Science* **331**, 1154 (2011).
- [34] P. Müller, K. W. Rogers, S. R. Yu, M. Brand, and A. F. Schier, Morphogen transport, *Development (Cambridge)* **140**, 1621 (2013).
- [35] R. Mateus, L. Holtzer, C. Seum, Z. Hadjivasiliou, M. Dubois, F. Jülicher, and M. Gonzalez-Gaitan, BMP Signaling Gradient Scaling in the Zebrafish Pectoral Fin, *Cell Reports* **30**, 4292 (2020).
- [36] M. Romanova-Michaelides, Z. Hadjivasiliou, D. Aguilar-Hidalgo, D. Basagiannis, C. Seum, M. Dubois, F. Jülicher, and M. Gonzalez-Gaitan, Morphogen gradient scaling by recycling of intracellular Dpp, *Nature* **602**, 287 (2022).
- [37] M. F. Lefebvre, N. H. Claussen, N. P. Mitchell, H. J. Gustafson, and S. J. Streichan, Geometric control of Myosin-II orientation during axis elongation, *eLife* **12**, 2022.01.12.476069 (2023).
- [38] O. Wartlick, A. Kicheva, and M. González-Gaitán, Morphogen gradient formation., *Cold Spring Harbor perspectives in biology* **1**, 10.1101/cshperspect.a001255 (2009).
- [39] Y. Wang, X. Wang, T. Wohland, and K. Sampath, Extracellular interactions and ligand degradation shape the nodal morphogen gradient, *eLife* **5**, 10.7554/eLife.13879 (2016).
- [40] A. Huang, C. Amourda, S. Zhang, N. S. Tolwinski, and T. E. Saunders, Decoding temporal interpretation of the morphogen bicoid in the early drosophila embryo, *eLife* **6**, 1 (2017).
- [41] A. C. Paré, A. Vichas, C. T. Fincher, Z. Mirman, D. L. Farrell, A. Mainieri, and J. A. Zallen, A positional Toll receptor code directs convergent extension in Drosophila, *Nature* **515**, 523 (2014).
- [42] M. A. Benton, M. Pechmann, N. Frey, D. Stappert, K. H. Conrads, Y. T. Chen, E. Stamatakis, A. Pavlopoulos, and S. Roth, Toll Genes Have an Ancestral Role in Axis Elongation, *Current Biology* **26**, 1609 (2016).
- [43] D. Jia, Q. Xu, Q. Xie, W. Mio, and W. M. Deng, Automatic stage identification of Drosophila egg chamber based on DAPI images, *Scientific Reports* **6**, 1 (2016).
- [44] H. Alégot, P. Pouchin, O. Bardot, and V. Mirouse, Jak-stat pathway induces Drosophila follicle elongation by a gradient of apical contractility, *eLife* **7**, 10.7554/eLife.32943 (2018).
- [45] D. D. Iwaki, K. A. Johansen, J. B. Singer, and J. A. Lengyel, Drumstick, bowl, and lines are required for patterning and cell rearrangement in the Drosophila embryonic hindgut, *Developmental Biology* **240**, 611 (2001).
- [46] M. L. Williams and L. Solnica-Krezel, Nodal and planar cell polarity signaling cooperate to regulate zebrafish convergence and extension gastrulation movements, *eLife* **9**, 10.7554/eLife.54445 (2020).
- [47] B. Steventon, F. Duarte, R. Lagadec, S. Mazan, J. F. Nicolas, and E. Hirsinger, Species-specific contribution of volumetric growth and tissue convergence to posterior body elongation in vertebrates, *Development (Cambridge)* **143**, 1732 (2016).
- [48] A. Kicheva, P. Pantazis, T. Bollenbach, Y. Kalaidzidis, T. Bittig, F. Jülicher, and M. González-Gaitán, Kinetics of morphogen gradient formation, *Science* **315**, 521 (2007).
- [49] A. Tiribocchi, R. Wittkowski, D. Marenduzzo, and M. E. Cates, Active Model H: Scalar Active Matter in a Momentum-Conserving Fluid, *Phys. Rev. Lett.* **115**, 1 (2015), [arXiv:1504.07447v1](https://arxiv.org/abs/1504.07447v1).
- [50] T. R. Kirkpatrick and J. K. Bhattacharjee, Driven active matter: Fluctuations and a hydrodynamic instability, *Phys. Rev. Fluids* **4**, 1 (2019).
- [51] B. Gao, Wnt Regulation of Planar Cell Polarity (PCP), *Current Topics in Developmental Biology* **101**, 263 (2012).
- [52] M. Merkel, A. Sagner, F. S. Gruber, R. Etournay, C. Blasse, E. Myers, S. Eaton, and F. Jülicher, The balance of prickle/spiny-legs isoforms controls the amount of coupling between core and fat PCP systems, *Current Biology* **24**, 2111 (2014).
- [53] S. S. Lienkamp, K. Liu, C. M. Karner, T. J. Carroll, O. Ronneberger, J. B. Wallingford, and G. Walz, Vertebrate kidney tubules elongate using a planar cell polarity-

- dependent, rosette-based mechanism of convergent extension, [Nature Genetics](#) **44**, 1382 (2012).
- [54] O. Ossipova, K. Kim, and S. Y. Soko, Planar polarization of vangl2 in the vertebrate neural plate is controlled by wnt and myosin ii signaling, [Biology Open](#) **4**, 722 (2015).
- [55] M. Ibrahimi, *Robustness of active anisotropic deformation in developing biological tissues*, [Ph.D. thesis](#), Aix-Marseille Université (2022), 2022AIXM0523.